Physical interpretation of time-varying StorAge Selection functions in a model hillslope via geophysical imaging of ages of water.

Antônio Alves Meira Neto[1,2]*, Minseok Kim[2], and Peter A. Troch[1,3]

[1]University of Arizona, Department of Hydrology and Atmospheric Sciences

[2] Institute of Climate Studies, Federal University of Espírito Santo, Vitória, ES, Brazil

[3] University of Arizona, Biosphere 2

*Corresponding author: antoniomeira@gmail.com

Key points

1. Electrical resistivity imaging was used to derive spatial distributions of water ages in a model hillslope.
2. Analysis of time-varying SAS functions indicated increasing release of younger water with decreasing storage.
3. Downward and upward soil saturation mechanisms were identified as causing the observed behavior.

ABSTRACT

Understanding transit times (TT) and residence times (RT) distributions of water in catchments has recently received a great deal of attention in hydrologic research since it can inform about important processes relevant to the quality of water delivered by streams and landscape resilience to anthropogenic inputs. The theory of transit time distributions (TTD) is a practical framework for understanding TT of water in natural landscapes but, due to its lumped nature, it can only hint at the possible internal processes taking place in the subsurface. While allowing for the direct observation of water movement, Electrical Resistivity Imaging (ERI) can be leveraged to better understand the internal variability of water ages within the subsurface, thus enabling the investigation of the physical processes controlling the time-variability of TTD. We estimated time variable TTD through the storage selection (SAS) framework following a traditional lumped-systems approach, based on sampling of output tracer concentrations, as well as through an ERI SAS approach based on spatially distributed images of water ages. We compared the ERI-based SAS results with the output-based estimates to discuss the viability of ERI at laboratory experiments for understanding TTD. The ERI-derived images of the internal evolution of water ages were able to elucidate the internal mechanisms driving the time-variability of ages of water being discharged by the system, which was characterized by a delayed discharge of younger water starting at the highest storage level and continuing throughout the water table recession.

1. Introduction

Water transit time (TT) is defined as the time spent from the moment water arrives at the land surface until it reaches the streams, a larger body of water, or is evaporated, and its estimation represents a fundamental challenge in hydrologic research. Knowledge about TT can inform a myriad of processes taking place in the subsurface, as it influences the overall equilibrium of weathering reactions (Maher, 2010, 2011) and release of nutrients (Brantley et al., 2007), while also serving as an indicator of catchment sensitivity to anthropogenic inputs (Landon et al., 2000; Turner et al., 2006).

The theory of transit time distributions (TTD) has been widely used as the mathematical framework to characterize TT at the catchment-scale. TTD theory considers a lumped representation of the hydrologic system, which is subject to input fluxes with known solute concentration that are modified by the TTD, yielding solute concentrations at the system's outlet. Although TTD have been traditionally studied under the assumption of steady-state conditions (Jury, 1982; Małoszewski and Zuber, 1982; Cvetkovic, 2011), surmounting evidence has been gathered towards its inadequacy to reproduce transport dynamics seen in natural landscapes, where steady-state is rarely if ever present (McGuire and McDonnell, 2006; McDonnell, 2010; Harman 2015). Recent convergence towards the development of time-variable TTD has been consolidated into the theory of StorAge Selection (SAS) functions (Botter et al., 2011; van der Velde et al., 2012; Harman, 2015; Rinaldo et al., 2015; Porporato and Calabrese, 2015). Within the SAS framework, the storage within a system is considered to be composed of water parcels having varying ages. The ranked storage selection function (rSAS, Harman, 2015) is one of the existing models proposed to apply SAS theory to quantify time-variable TTD at the pedon and catchment-scale (Harman, 2015; Kim et al., 2016; Wilusz et al., 2017; Rodriguez et al., 2018). Within the rSAS framework, the age-ranked storage (S_T) is the variable that describes the amount of storage having ages smaller than a certain value T, while the water that leaves the system at a certain moment (e.g. streamflow and evapotranspiration) is selected from storage through a storage selection function (Ω_Q).

As for the steady-state case of TTD, the estimation of the rSAS variables for real-world catchments follows an inference procedure in which information on water and solute fluxes in and out of the system is needed, together with a prior assumption of the shape of Ω_Q. However, the direct observation of time-variable TTD with no prior assumption about its shape is possible under controlled experimentation: the Periodic Tracer Hierarchy method (PERTH, Harman and Kim, 2014) is a tracer experiment conceived for the direct observation of time-variable transit time distributions. The method requires a Periodic Steady State (PSS) to be imposed to the system, which allows for breakthroughs from multiple tracer injections to be quantified. Kim et al., (2016) applied the PERTH method to observe the time-variability of Ω_Q at a $1m^3$ sloping soil lysimeter subject to a 24-hour hydrologic cycle. They were able to verify that an inverse-storage effect (ISE) characterized the transport dynamics within the model system: under high-storage conditions, higher fractions of young water were proportionally released, whereas larger fractions of older water were released at lower storages.

While lumped-system approaches are useful to represent transport processes within hydrologic systems, they cannot provide spatially variable information of processes taking place within the subsurface. Therefore, additional methods that account for the internal variability of flow paths are necessary to fully investigate the temporal variability seen in natural landscapes and also promote a physical interpretation of the results arising from lumped approaches (Van der Velde et al., 2015; Rinaldo et al., 2015). Studies making use of physically based models have been proven useful to elucidate the mechanisms behind the time-variability of TTD. Ameli et al., (2016) used an integrated subsurface flow and advective-dispersive particle movement model to assess the role of subsurface architecture on flow pathways and TTD of a hillslope in Sweden. They found macro-scale heterogeneity, vertical distribution of saturated hydraulic conductivity and location of the water divide to significantly impact the structure of TTD. Yang et al., (2018) used a 3D fully coupled surface-subsurface model with random-walk particle tracking in a combined investigation of flow paths and SAS theory components from an agricultural catchment in central Germany. Their analysis suggested a shift in the age of discharged water from younger towards older when transitioning from a wet towards dry period. They found the change from fast and shallow flow paths towards deeper flow paths to explain the observed shift. Pangle et al., (2017) expanded on the results from Kim et al., (2016) by simulating the hydrologic fluxes and transport for the same experimental lysimeter through a 2D physically based model. That study suggests that the rapid mobilization of water close to the soil surface by a rising water table to result in the observed ISE.

The relationship between TTD variability and the underlying subsurface processes inferred through physically based modeling are however subject to modelling uncertainties and need empirical validation. Geophysical methods have been widely used to monitor tracer transport over a broad range of scales in a non-invasive way (Binley et al., 2015). Among existing geophysical methods, Electrical Resistivity Imaging (ERI) has been consolidated as a practical tool for investigating solute transport in the subsurface (Binley et al., 1996; Kemna et al., 2002; Singha and Gorelick, 2006; Koestel et al., 2008; Wehrer and Slater, 2014). Although the tracking and quantification of tracer movement through the subsurface can yield invaluable insight on water flowpaths, no study has so far used it for the direct quantification of TT.

Here, we present an ERI-based extension of the PERTH method for the quantification of the SAS theory components at the laboratory scale. This study reports the results of the application of the PERTH method to a 1m^3 sloping soil lysimeter following two different approaches: 1) We estimated the rSAS components (S_T and Ω_Q) through a lumped approach by collecting samples of conservative tracers from irrigation and discharge, and 2) we used spatial estimates of solute concentration from ERI images to provide a spatial representation of water ages within the subsurface while also attempting to estimate ERI-derived rSAS components. With the aid of additional hydrometric data, this combined approach was leveraged to provide a physical interpretation for the lysimeter's internal functioning, and the resulting lumped estimates of transport as seen in the rSAS functions.

2. Materials and Methods

2.1. The MiniLEO Lysimeter

The miniLEO (**Figure1-A**) is a 10-degree sloping soil lysimeter with $1m^3$ capacity (0.5 m x 2.0 m x 1.0 m) located at the University of Arizona Biosphere 2 facility in Oracle, Arizona. The lysimeter is a small-scale replicate of the Landscape Evolution Observatory (LEO) artificial hillslopes (Pangle et al., 2015) constructed at the same facility. The interior walls and floor of the lysimeter are coated with a non-conductive abrasion-resistant waterproofing system (DuralDeck, Euclid Chemical Company). The miniLEO rests on 4 load cells (Honeywell Model 41 Load Cell) and is equipped with a sprinkler-based irrigation system composed of multiple sprinkler heads (not shown) that can be adjusted to deliver rain intensities ranging from 10 to 30 mm/h. For this experiment, the irrigation system was adjusted for a single rain intensity (14mm/h, using 3 sprinkler heads) and multiple trial runs were performed to achieve a homogenous rainfall distribution over the soil surface. The lower-right end wall of the lysimeter act as a seepage face (at atmospheric pressure, no suction is applied at this boundary condition), and is composed of a perforated plastic sheet separated from the basaltic soil by a 10 cm basalt gravel layer. Seepage water is collected at a gutter and is routed to a tipping bucket (ONSET HOBO model RG3), allowing for the computation of the volumetric discharge out of the system. Discharge samples were collected at each hour throughout the course of the experiment. Vertically arranged Prenart® suction lysimeters at 5 different depths (5, 20, 35, 50 and 85 cm) are located along 3 sampling verticals (at y = 0.65, 1.25 and 1.85m, **Figure 1-A**). Suction lysimeters are routed to an airtight acrylic box (not shown) containing reusable plastic veils for sample collection at each corresponding location. The acrylic box is connected to a vacuum pump adjusted for -0.5 Bar suction, allowing for simultaneous sample collection from all locations. Two sensors were co-located with the suction lysimeters (with an approximate separation of 5 cm in the x-direction): Decagon® MPS-2 matric potential sensors, used to provide temperature readings, and Decagon® 5TM for measurements of volumetric soil water content. Additionally, two Campbell CS451 pressure transducers were installed at the lysimeter floor (triangles in **Figure 1-A**).

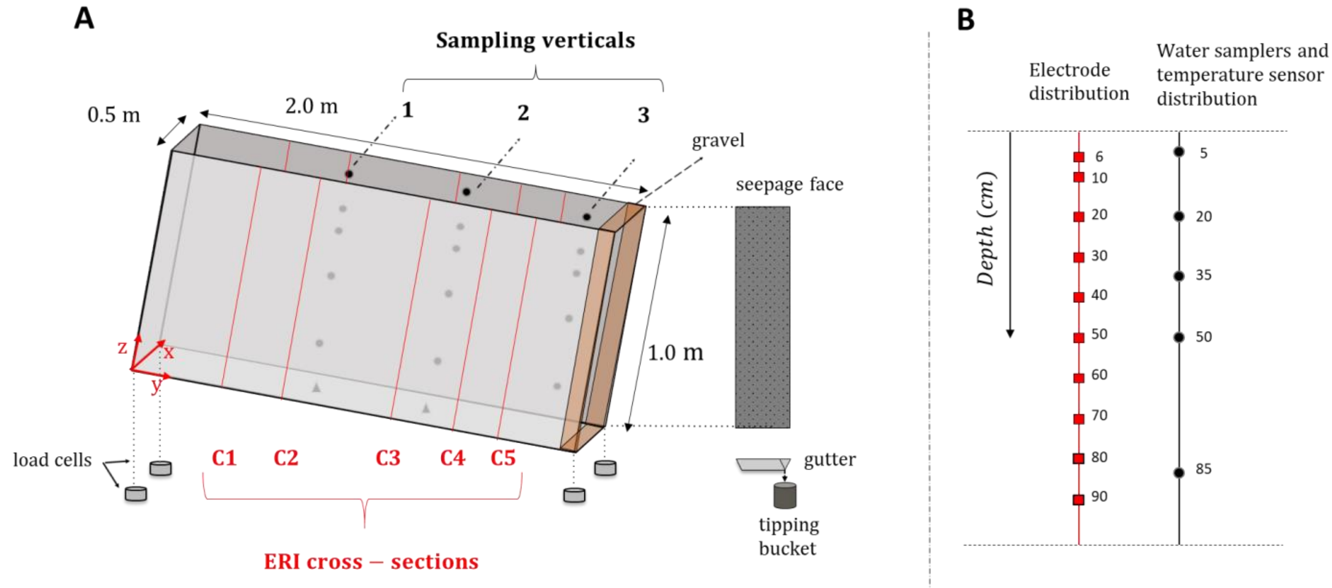

Figure 1. Schematic view of the miniLEO soil lysimeter. A- Overview of the lysimeters dimensions, sampler and sensor locations, ERI verticals (red lines) along the walls and overall instrumentation. ERI measurements were taken at verticals from opposite sides of the lysimeter, producing cross-sectional images (cross-sections C1 through C5). Triangles represent Campbell CS451 pressure transducers. The Coordinate system (x, y and z directions) used throughout the text is highlighted in the lower end of the lysimeter. The location of the vertical gravel layer is shown in brown. Aside from this layer, the lysimeters volume was filled with the basaltic loamy sand. A metallic structure (not shown here) responsible for supporting the lysimeters weight and keeping it at a 10º angle did not allow for a uniform distribution of ERT verticals along the y-axis. B- Depth distribution of stainless-steel electrodes (red) and water samplers (Prenart ® suction lysimeters – black circles).

The material within the miniLEO is a basalt tephra extracted from a deposit in northern Arizona that was further ground on site to a loamy sand texture. The final texture distribution was achieved by sieving and remixing different size fractions of the original basalt so that a larger percentage of fines could be achieved (Dontsova et al., 2009). This procedure led to a final texture consisting of approximately 85% sand-size particles (≥ 50 and < 2000 µm), 12% silt-size particles (≥ 2 and < 50 µm), and 3% clay-size particles (< 2 µm). The material, herein referred to as basaltic soil, is the same as in the LEO hillslopes and was chosen as part of the investigation of the coevolution of soils and landscape complexity mediated by physical and biogeochemical processes (Pangle et al., 2015). The intended low content of fine particles (approx. 32 g kg^{-1}) should allow for an easier detection of incipient secondary mineral formation (Pohlman et al., 2016). Even though clay-sized particles are present in the basaltic soil, no secondary minerals were observed as part of the basalt's mineralogical composition (Dontsova et al., 2009; Pangle et al., 2015; Pohlman et al., 2016). The basaltic soil was added to the lysimeter through a procedure consisting of sequentially adding 32 cm increments of loose soil, which were then compacted to 25cm. During this procedure, the first 10 centimeter from the seepage face were occupied by the original gravel-size basaltic tephra to serve as a drainage layer.

10 ERI verticals (located at y = 0.25, 0.55, 1.1 1.4, and 1.63) containing 10 electrodes each are distributed along both walls of the lysimeter, as seen in **Figure1-A** and **B**. The location of the ERI-verticals was chosen in order to avoid overlap with sensor-verticals and also due to inaccessibility of certain portions of the lysimeter wall that were blocked by the metal structure used to keep the lysimeter at its 10-degree slope (see **Figure S1-A** for more details). This layout allows for acquisition of 5 cross-sectional resistivity images at different locations along the y-direction, hereafter referred to as cross-sections C1 through C5, in which the number 1 represents the upper most cross-section (y = 0.25 m) and 5 the lower most (y = 1.63 m). The electrode distribution of each vertical follows a 10 cm spacing interval, with the exception of the first electrode position (**Figure1-B)**. The electrodes are 3 mm diameter stainless steel rods secured by plastic cable glands installed through orifices in the lysimeter walls. The electrodes were installed prior to the soil packing and the orifices were sealed with the same non-conductive water-proofing system used internally (see **Figure S1-B** for more details).

2.2. rSAS Theory

The ranked storage selection theory (rSAS) is one of the existing variations within the SAS framework (Botter et al., 2011; Rinaldo et al., 2015; van der Velde et al., 2012). In this theory, the system is assumed to be a single control volume, subject to a precipitation $J(t)$ input flux and the output fluxes from discharge $Q(t)$ and evapotranspiration $ET(t)$. At any moment t, the ages ($\mathcal{T}$) of water in storage can be represented by the residence time distribution $P_S(T,t)$, representing the cumulative distribution of ages within the system. The fluxes in and out of the system will alter the structure of $P_S(T,t)$ over time, through the cumulative backwards transit times distributions (bTTD) of discharge $\overleftarrow{P_Q}(T,t)$ and evapotranspiration $\overleftarrow{P_{ET}}(T,t)$. We can write the continuity equation of ages and mass within the system as (Harman et al., 2015):

$$\frac{\partial S_T(T,t)}{\partial t} = J(t) - Q(t)\overleftarrow{P_Q}(T,t) - ET(t)\overleftarrow{P_Q}(T,t) - \frac{\partial S_T(T,t)}{\partial T}, \qquad (1)$$

where the age-ranked storage, $S_T(T,t)$ represents the actual storage having ages $\mathcal{T} < \mathrm{T}$:

$$S_T(T,t) = S(t)P_S(T,t) \quad (2)$$

where $S(t)$ represents storage, in mm. Equation 1 shows that S_T is modified in time by the increase in storage from precipitation (assumed to have age equal to zero), the decrease in storage with age selection being determined from $\overleftarrow{P_Q}(T,t)$ and $\overleftarrow{P_{ET}}(T,t)$ and the ageing of water within the system as $\frac{\partial S_T(T,t)}{\partial T}$. While difficult to parameterize, the terms $\overleftarrow{P_Q}(T,t)$ and $\overleftarrow{P_{ET}}(T,t)$ have been found to be more conveniently expressed as cumulative functions of S_T:

$$\Omega_{\mathrm{Q}}(S_T,t) = \overleftarrow{P_Q}(T,t) \quad (3)$$

$$\Omega_{\mathrm{ET}}(S_T,t) = \overleftarrow{P_{ET}}(T,t) \quad (4)$$

where Ω_Q and Ω_{ET} are the rSAS functions of discharge and evapotranspiration. The rSAS functions therefore represent the outflux selection from the age-ranked storage, and the transformation from $P(T,t)$ to $\Omega(\mathrm{S_T},t)$ is possible due to the direct mapping between T and S_T. We assume the soil evaporation throughout the experiment to be negligible, as we attempted to keep such flux at a minimum by shutting off air circulation fans, and keeping the air inside the facility at a reasonably high relative humidity values. Such assumption was similarly taken in the studies from Kim et al., (2016, 2020), performed in the same facility, for which meaningful estimates of the SAS components were still obtained.

2.3. PERTH Experiment and Retrieved rSAS Components.

The experiment is an application of the Periodic Tracer Hierarchy (PERTH) method (Harman and Kim, 2014), conceived for the direct observation of time-varying transit time distributions. A short description of the method is provided here, and a more in-depth discussion of the method can be found in Kim et al. (2021).

Through the PERTH method, it is possible to quantitatively separate overlapping (in time) breakthrough curves resulting from repetitive injections of the same tracer. Breakthrough curves from each injection are assumed to result from an instantaneous injection of a conservative tracer, providing realizations of the forward transit time distribution (fTTD, aka system response function) (Niemi, 1977). For a system that is not in steady state, that realization of the fTTD would be conditional on the time of injection t_i, as indicated in the notation commonly used for this probability distribution: $\vec{p}(t - t_i|t_i)$. By repeated injections of the same tracer in a system under unsteady-state conditions, additional realizations of the fTTD are obtained, with each of them being uniquely affected by the hydrological conditions that existed at the time of injection t_i, and thereafter. Although this can lead to a direct quantification of the time dependence of fTTDs, the time necessary for its execution would make it infeasible, since for each injection we would require complete flushing of the tracer. The PERTH method makes it possible to directly observe time-variable fTTDs over a much shorter experimental period.

For the application of the PERTH method, a periodic steady state (PSS) condition (Harman and Kim, 2014) is required, which can be achieved by the application of an irrigation cycle that is systematically repeated. Under PSS conditions, the system will be forced to repeat the same internal states (total storage and spatial moisture content distribution) and outputs (discharge through the outlet). The PERTH method consists in the sequential injection of different tracers while the system is experiencing PSS conditions and its final goal is the estimation of the time-variability of rSAS components within one cycle.

In this study, the PSS experiment was conducted between June 22nd and July 21st 2018 and consisted of the repetition of an irrigation schedule within 48 hour cycles (t_c = 48 h, following the notation of Harman and Kim, (2014)). Each cycle consisted of two 3-hour-long irrigation pulses separated by a 2-hour period, both having a target intensity of 14 mm/hr. The pulses were applied from 8:30 to 11:30 and from 13:30 to 16:30 of the first day, while no irrigation occurred during the second day (**Figure 2**). Seven irrigation cycles occurred before the introduction of tracers in order to bring the system to a PSS.

We used chloride (dissolved LiCl in irrigation water), as a reference tracer (C_R) and deuterium (^{2}H) and oxygen-18 (^{18}O) as probe tracers (C_0 and C_1, respectively). A whole cycle with tracer-labeled water was applied once PSS was achieved: The first pulse was labeled with C_R and C_0, while the second pulse contained C_R and C_1. A value of $10000\ \mu\mathrm{mol/L}$ of chloride was chosen for C_R (reference tracer), while the values of δ^2H and δ^{18}O of 250 ‰ and 15 ‰ (VSMOW) were selected for C_0 and C_1 (probe tracers) respectively. Discharge water samples were collected hourly and analyzed for δ^2H and δ^{18}O relative to Vienna Standard Mean Ocean Water (VSMOW) using a Los Gatos Research DLT-100 Laser Spectrometer. We obtained chloride concentrations from electrical conductivity measurements of discharge water samples using a linear relationship calibrated in the laboratory ($r^2 = 0.99$) relating chloride concentration to electrical conductivity. Following the tracer application, additional irrigation cycles were scheduled until water samples at the sampling locations reached pre-injection conductivity values.

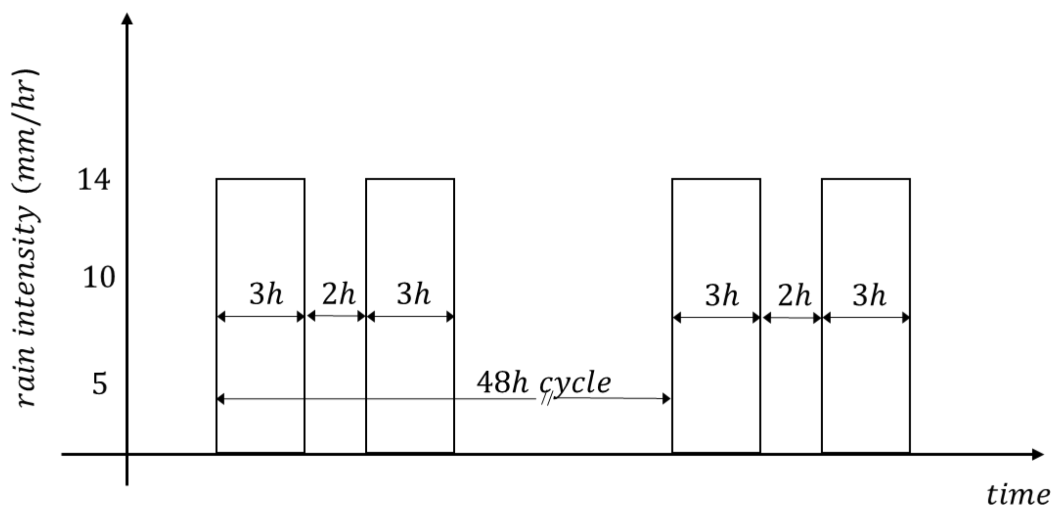

Figure 2. Schematic of the 48 hours cycle of rain application imposed at the miniLEO lysimeter.

2.4. ERI-based Estimation of Internal Ages of Water and rSAS Components

We estimated the internal distribution of ages of water within one PSS cycle by converting ERI-based images of soil bulk electrical conductivity (σ_b, in $\mu S/cm$) into images of fluid conductivity (σ_f, in $\mu S/cm$) which were then converted to Cl concentration ($\frac{\mu mol}{L}$). The ERI surveys produced cross-sectional images at the 5 y-direction locations of the ERI verticals (i.e. 2D panels across the x-z dimensions, **Figure 1A**), which were extrapolated to produce lysimeter-wide panels (2D panels across y-z dimensions, **Figure 1A**).

A more detailed description of the ERI application is presented in the following sections. In **Section 2.4.1** we provide details on the acquisition, pre-processing and inversion of ERI data. **Section 2.4.2** elaborates on the procedure to extract images of estimated σ_f across the soil lysimeter and its conversion into Cl concentration images across the lysimeters length. Finally,

Section 2.4.3 describes how the estimated Cl concentrations were converted into images of water ages across one representative PSS cycle.

2.4.1. Collection, Preprocessing and Inversion of ERI Data.

Measurements of soil resistance (R −ratio of measured voltage between a pair of electrodes by the current injected between another pair or electrodes) were performed using the 8 channel Supersting R8 (Advanced Geosciences Inc.) electric resistivity meter. We followed a time-lapse cross-borehole survey designed to obtain 2D cross-sectional images at the 5 locations along the y-direction. 2D cross-borehole configurations allow for quick image acquisition and have been widely used for studies of solute transport and plume migration in a variety of environments (Slater et al., 2000; Kemna et al., 2002; Looms et al., 2008; Perri et al., 2012; Bellmunt et al., 2016). A skip-dipole (Slater et al., 2000) measurement scheme with 2 and 3 electrode distances as the assigned skip, representing 248 measurements to be taken per cross-section (including reciprocals) was chosen. A survey consisted of repeating the same scheme from cross-sections 1 through 5, resulting in a total of 1240 measurements per run. A total of 1190 surveys were performed between June 22nd, 2018, and July 21st 2018, with each survey taking approximately 35 minutes. Poor soil-electrode contact during dry days allied to the low-conductivity water used in the rain pulses made it impossible for all readings to be taken at all surveys. This led to a reduction of the total measurements to an average of 1182 per survey (237 measurements per cross section, in average).

An error analysis procedure was conducted prior to the inversion. We first excluded obvious outliers by removing measurements with reciprocal error (ϵ_{recip}, Slater et al., 2001) greater than 5%, which resulted in a 7% reduction of the initial number of measurements. Following that, we estimated an error model for each survey in order to estimate weights to be used in the inversion (Slater et al. 2001, Koestel et al., 2008, Wehrer and Slater, 2015). This was done by binning the reciprocal measurement ($\overline{\mathrm{R}}$) values in 10 classes with increasing order of magnitude and fitting a linear relationship between binned values of $\bar{R}$ and ϵ_{recip}, from which the slope and intercept were retained.

The surveys were inverted with the code R3t (Binley, 2013), which estimates the spatial distribution of resistivities from measured potential and current values. We used the software Gmsh (Geuzaine and Remacle, 2009) to generate a three-dimensional finite element mesh consisting of 20640 tetrahedral elements with characteristic length of 5 cm. A time-lapse ERI inversion scheme based on the difference regularization method of Labrecque and Yang (2001) was used in this study. This method allows for faster convergence and tends to minimize systematic errors. First, a reference dataset to be used as the a priori model for subsequent inversions is inverted according to the following objective function:

$$\Psi_d = (\mathrm{W_d}[\boldsymbol{d} - f(\boldsymbol{m})])^2 + \alpha(\mathrm{W_m}\boldsymbol{m})^2, \tag{5}$$

Where $\boldsymbol{d}$ is the vector of measured resistances (Ohm), $\boldsymbol{m}$ is the model vector of resistivities $(Ohm.m)$, $f(\boldsymbol{m})$ is the forward solution of the resistances, $\mathrm{W_d}$ is a matrix containing the data weights, $\mathrm{W_m}$ is the roughness matrix, which is used to generate a smooth solution by penalizing differences between adjacent values of modelled resistivities and α is a smoothing parameter, which assigns a weight to the second term of the objective function. The first term of the objective function represents the misfit between modelled and measured data, while the second is a measure of smoothness of the forward model. After the reference dataset is inverted, the data vector $(\boldsymbol{d})$ is modified for the subsequent datasets as:

$$\boldsymbol{d} = \boldsymbol{d}' - \boldsymbol{d_{ref}} + f\left(\boldsymbol{m_{ref}}\right) \tag{6}$$

Where $\boldsymbol{d}'$ is the vector of measured resistances at a subsequent time, $\boldsymbol{d_{ref}}$ represents the measured resistances used in the reference dataset and $f(\boldsymbol{m_{ref}})$ is the forward solution of the reference dataset. A new objective function based on the minimization of the differences between current and reference datasets and the smoothness term is then calculated:

$$\Psi_d = (\mathrm{W_d}[\boldsymbol{d} - f(\boldsymbol{m})])^2 + \alpha\left(\mathrm{W_m}\left[\boldsymbol{m} - \boldsymbol{m_{ref}}\right]\right)^2, \tag{7}$$

Two-dimensional cross-sectional images of bulk resistivity were extracted from the inverted three-dimensional fields of resistivities and further converted to bulk conductivity values $(\sigma_b, \mu S/cm)$. Since electrical conductivity is influenced by temperature (Campbell et al., 1948), the resulting conductivity values were corrected to a reference temperature by:

$$\sigma_b\left(T_{ref}\right) = \frac{\sigma_b(T)}{1 + 0.02\left(T - T_{ref}\right)} \tag{8}$$

Where T is the in-situ temperature provided by the MPS2-2 matric potential sensors (see Section 2.1), and T_{ref} is a reference temperature (25 °C). Measurements from the co-located temperature sensors were spatially interpolated and extrapolated to generate spatial temperature estimates at the cross-sections at the different times.

2.4.2. Spatial and Temporal Estimates of Cl Concentration

The petrophysical relationships between soil bulk electrical conductivity/resistivity and its controlling variables differ for soils with and without clay minerals. The formulations presented in this section provide a method for using the PSS imposed throughout the PERTH experiment to extract the fluid conductivity assuming a soil with negligible clay formation, as is the case for the basaltic soil inside the miniLEO. A slightly modified experimental procedure can be executed in the case of soils with clay minerals, and its description is provided as supporting information (**Text S1**).

For non-conductive soils, the soil bulk electrical conductivity ($\sigma_b, in\ \mu S/cm$) can be explained as a function of the conductivity of the soil water (σ_f), porosity (ϕ) and water-saturation (S), and is described by Archie's law (Archie, 1942) as:

$$\sigma_b = \sigma_f \phi^m S^n \tag{9}$$

where m is the cementation exponent, and n is the saturation exponent. It can be seen that σ_b estimated through ERI surveys are controlled by multiple variables. In order to convert the estimates of σ_b into fluid conductivity (σ_f), estimates of soil porosity (ϕ), water saturation (S), and eventually soil-surface conductivity (σ_s) are needed. This poses additional challenges for the quantitative assessment of solute transport through ERI methods. These circumstances limit ERI applications to steady-state conditions when the exponents m and n are unknown (Binley et al., 1996; Slater, 2001; Alumbaugh et al., 2004; Koestel et al., 2008), or will require the knowledge of both soil parameters and moisture states through time for unsteady-state conditions (Wehrer and Slater, 2015).

A simple approach that takes advantage of the repeatability seen at PSS conditions can be developed that allows for a quantitative characterization of solute transport under unsteady state conditions with spatially varying degrees of saturation. Under PSS, the variables in equation 9 become a function of the time relative to the beginning of a cycle (t^*):

$$\sigma_b(t^*) = \sigma_f(t^*)\phi^m S(t^*)^n. \tag{10}$$

The internal states and outputs achieved within a PSS-cycle will result from an interplay between internal properties (porosity, hydraulic conductivity, and retention characteristics) and the input sequence. Considering a soil lysimeter subject to an irrigation schedule, moisture states and fluxes can vary from saturated to unsaturated conditions both in space and time depending on the intensity and duration of the imposed irrigation sequence.

Assuming that PSS conditions have been achieved, and that water with known background tracer concentrations and conductivity has been used, the system will be in what we define as a “warmup” (w) period. The response of a warmup cycle as:

$$\sigma_b(t_w^*) = \sigma_f(t_w^*)\phi^m S(t_w^*)^n, \tag{11}$$

where t_w^* is the time relative to the beginning of the warmup cycle. Once PSS is reached, the progression σ_b within a cycle should be repeated at every cycle. The estimation of a representative warmup cycle can therefore be taken from any cycle within PSS conditions, or an average of all warmup cycles to account for between cycle variability that can potentially arise due to failure in repeating the exact input sequence. Following that, an “injection” cycle can be performed, in which water with contrasting concentrations (and conductivity) is applied. Subsequent cycles are then imposed with the previously used background concentrations until tracer recovery is satisfactorily achieved. For the cycles from injection until the end of recovery the soil-bulk conductivity can be written as:

$$\sigma_b(t_k^*) = \sigma_f(t_k^*)\phi^m S(t_k^*)^n \tag{12}$$

where t_k^* is the time relative to the beginning of the k^{th} cycle (k = 1 representing the injection cycle). By dividing each injection or recovery cycles response by the warmup-cycle response, the following expression can be written:

$$\frac{\sigma_b(t_k^*)}{\sigma_b(t_w^*)} = \frac{\sigma_f(t_k^*)}{\sigma_f(t_w^*)} \cdot \frac{\phi^m S(t_k^*)^n}{\phi^m S(t_w^*)^n}, \tag{13}$$

Since the term $\phi^m S(t)^n$ is the same for all cycles, we arrive at:

$$\sigma_{rat}(t_k^*) = \frac{\sigma_b(t_k^*)}{\sigma_b(t_w^*)} = \frac{\sigma_f(t_k^*)}{\sigma_f(t_w^*)} \tag{14}$$

where σ_{rat} is the ratio between bulk conductivities from injection or recovery cycles and that of the warmup cycle. Assuming that the pore-water conductivity throughout a warmup cycle, $\sigma_f(t_w^*)$, can be estimated, equation 14 provides a solution for σ_f at any arbitrary time t.

ERI-based values of concentration (C_{Cl}) were obtained by converting σ_f into values of concentration using a relationship between chloride concentration ($\mu mol/L$) and electrical conductivity ($\mu S/cm$) from soil-water samples using a linear relationship calibrated in the laboratory ($r^2 = 0.99$). We produced depth-averaged profiles of C_{Cl} at 10-cm spacing for visual assessment of chloride breakthroughs. For evaluation of the results, values of $C_{Cl,Obs}$ from the 3 water sampling verticals were superimposed onto the ERI-cross sections by linear interpolation, while C_{Cl} values were averaged at the equivalent locations. Details on depth-profile evaluation of the results are presented as supporting information (**Text S2, Figures S2 and S3, Table S1**).

Finally, 2-dimensional (along the y-z direction) panels of chloride concentration starting from the injection cycle and onwards were created based on the spatial interpolation of depth averaged profiles across the ERI-domain. Following that, warmup-cycle field of conductivities, spatially interpolated from the suction cups were subtracted from the injection and recovery cycle panels to yield a final sequence of Cl-breakthrough panels.

2.4.3. Ages of Water within a PSS Cycle

We estimated the spatial distribution of water ages within one PSS cycle using the spatial distributions of solute concentration from the tracer injection and subsequent irrigation cycles. For each time-step t, with $t = 0$ being the moment of the injection, the observed fraction of water from the injection was estimated as:

$$f_t = \frac{C_{Cl}(t)}{C_{\mathrm{In}}}, \tag{15}$$

where C_{In} is the concentration of the injected tracer. Since the moment of each image is known, f_t can be interpreted as the fraction of water having age equal to t. This resulted in estimates of f_t throughout 8 irrigation cycles (cycles 8 through 15 as seen in **Figure 3**), leading to observed fractions of water with ages up to 384 hours (8 cycles times 48 hours per cycle).

The PSS conditions imposed on the system implies that each irrigation pulse will lead to the same internal response, allowing for the assumption that the tracer progression observed since the injection cycle will be the same for each subsequent non-tracer-labelled cycle. Therefore, the last cycle will contain water having ages from the time of the injection up to the maximum observable age, in this case, 384 hours. We refer the last cycle hereinafter as the *representative cycle*. Since the chloride tracer was added throughout 2 pulses, the determination of the ages during the-injection period (ages from 1 to 8 hours) was not possible. Therefore, we assigned an average age of 4 hours for the water being injected during first 8 hours of the experiment.

The superposition of sequential tracer injections leads to the possibility for a point within the domain to be assigned different values of f_t. That occurs due to two main reasons: (i) the same point might contain some remaining fraction of water from a previous irrigation event when water from a new irrigation event is applied, and (ii) the ERI estimation of chloride concentration are subject to a smoothness arising from the inversion procedure. Therefore, at any specific moment within the representative PSS cycle, a single location might have water with varying ages. For the visual assessment of the spatial distribution of water ages within a representative cycle, we assigned for each pixel the age $\mathcal{T}^*$, representing the most frequent age (i.e., the age $\mathcal{T}$ with the higher f_t).

2.4.4. ERI-Based Estimation of SAS Theory Components

Once the internal distribution of ages within the representative PSS cycle was obtained, we followed with the estimation of the age-ranked storage (S_T). As noted previously, S_T represents the volume of water that has age less than or equal to T, with T being the time spent from the moment of entry up to the current time t. We combined the interpolated images of soil water content from the in-situ sensors with those of f_t for each moment t. We first estimated the age ranked-storage density $s_T(\mathcal{T}, t)$, by calculating at each pixel the product between storage and the fraction of water having age $\mathcal{T}$:

$$s_T(\mathcal{T}, t) = \sum v_{i,t} \cdot f_{t=\mathcal{T}}\,, \tag{16}$$

Where v_i is the volume of storage of a pixel i (mm), t is the time within the representative cycle (1 through 48), and $f_{\mathcal{T},t}$ is the assigned fraction of water having the age $\mathcal{T}$ at the same moment. v_i was estimated as the product of the volumetric water content at a pixel and its storage capacity (mm). We followed by estimating S_T as:

$$S_T^*(\mathcal{T},t) = \sum_{a=0}^{\mathcal{T}} s_T(\mathrm{a},t) \tag{17}$$

where the * symbol denotes ERI-based estimate. Following that, we estimated the storage selection function (Ω_{Q^*}) by first calculating the cumulative sum of the differences between the $s_T(\mathcal{T},t)$ vectors from each time-step, normalized by the change in storage between time-steps:

$$\Omega_{Q^*}(S_T^*(T,t),t) = -\frac{S_T^*(\mathrm{T},t+\Delta\mathrm{t}) - S_T^*(\mathrm{T}-\Delta\mathrm{T},t)}{\Delta\mathrm{t}}/Q^* \tag{18}$$

Where Q^* represents the total change in storage within the ERI surveyed domain over time, computed as:

$$Q^* = \frac{\sum v_{i,t+1} - \sum v_{i,t}}{\Delta t} \tag{19}$$

3. RESULTS

3.1. Hydrologic Assessment of the Experiment

The overall progression of the experiment can be seen in **Figure 3**. Seven warmup cycles occurred prior to the injection (8th cycle), followed by another 8 recovery cycles. **Figure 3A** shows the irrigation intensity (I) applied through the several pulses as well as measured seepage-face discharge (Q), whereas the load-cell mass changes are shown in **Figure 3B**. The estimated mean rainfall intensity was 13 mm/hr per pulse, with a standard deviation of 3 mm/hr (Coefficient of variance of 23%). Such variability occurred due to malfunctioning of the micro-controller that adjusts the pressure at the inlet of the tubbing system that distributes water to the sprinklers. The resulting spatial distribution resulted in higher intensities closer to the seepage face, where the average intensity at the upper third was approximately 10 mm/hr, followed by 12 and 15 mm/hr at middle-slope and seepage face thirds respectively. Even though the system quickly reached an oscillatory pattern from cycle #1, as seen in the variations in mass (**Figure 3B**), additional cycles were performed due to the issues mentioned previously. Electrical issues within the data-logging system during the cycles 1 and 3 led to poor estimation of mass and discharge values.

Figure 3C shows the tracer breakthroughs for chloride, ^{2}H and ^{18}O (*"C*), taken concentrations normalized by their injection and background values. The two irrigation pulses containing the tracers as described in **2.3** are depicted as two vertical yellow bars (not in scale, simply for illustration of the moments of the injection). A delayed tracer response can also be identified where the discharge conductivity is seen to increase after the first cycle of the recovery period (Cycle 9, day 2 in **Figure 3C**). It is also possible to see that both ^{2}H and ^{18}O were not detected in the same quantities as chloride, suggesting an imperfect tracer recovery of both tracers when compared to chloride. We were not able to define the actual cause for this issue, but a possible reason could have been an incorrect amount of tracer added to the irrigation system.

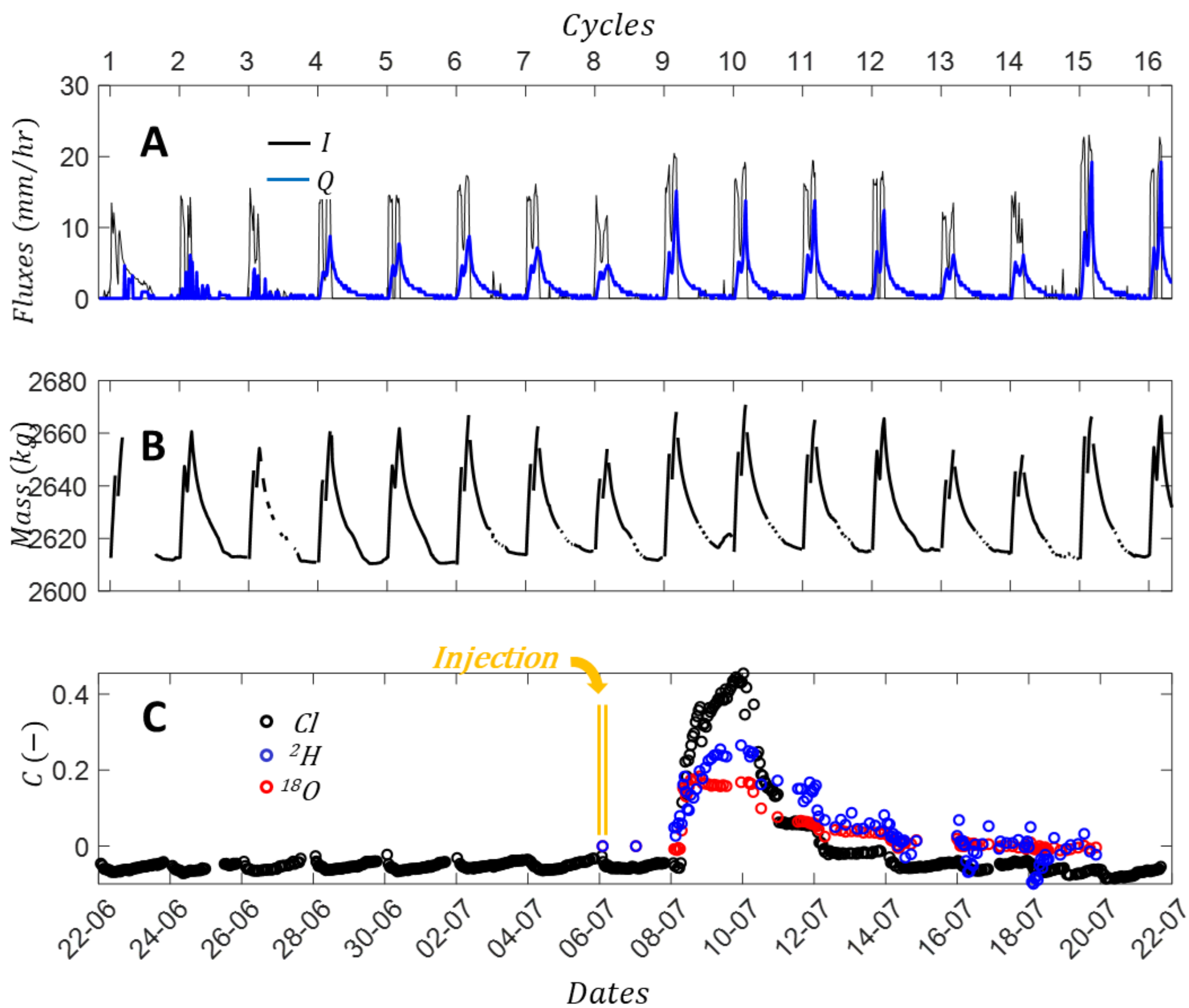

Figure 3. Hydrologic progress of the miniLEO lysimeter under a periodic steady state throughout the experiment. A- Irrigation (mm/hr) sequence applied throughout the experiment (black) and discharge (mm/hr) from the lysimeters seepage face (blue). B- Mass variations (kg) registered through the load cells indicate the increase in mass due to irrigation pulses and drainage periods. Equipment failure during the cycles 1 and 3 were responsible for missing values of mass and poor estimates of discharge for those periods. C- Normalized Concentrations for discharge fluxes.

Additional insights on the hydrologic processes within a cycle can be gained by analyzing both external and internal responses. **Figure 4A** shows the average responses of irrigation, discharge, and storage within the 48-hour cycle. It is possible to see the double peaked response in storage and discharge resulting from the sequential irrigation pulses, followed by a recession period. **Figure 4B** shows the approximate water table location at the instants 3, 5, 8, 16 and 48h. The water tables were obtained by linearly interpolating the observed values from the two pressure transducers (**Figure 1A**). While initially absent, the water table rises to a first peak at t = 3h, followed by a quick recession due to the absence of rainfall between t = 3h and t = 5h. With the end of the second irrigation pulse, the water table reaches its second peak at t = 8h, which is followed by a recession (see t = 16h) and the absence of a water table characterizing the initial conditions of the cycle.

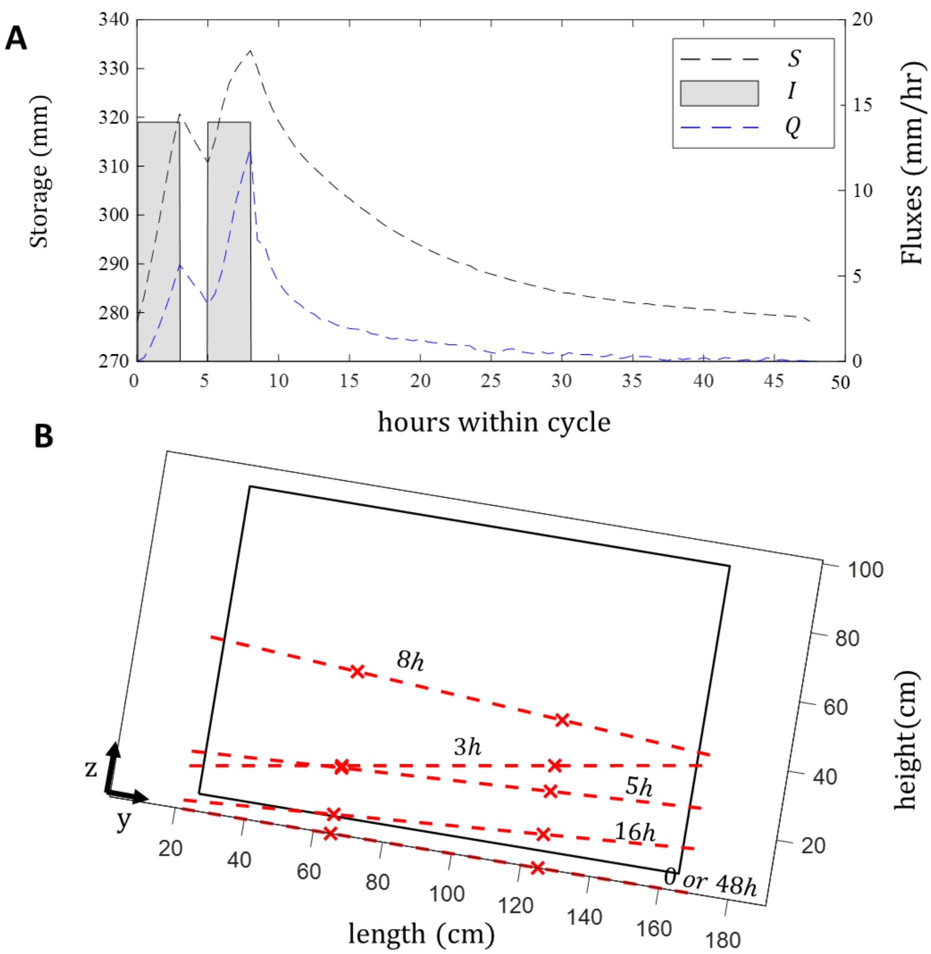

Figure 4. Characteristic (average) hydrologic responses within one cycle. A - Sequence of two 2-hour long irrigation pulses (gray bars) separated by a 2-hour period resulting in increasing storage (black dashed line) and discharge (blue dashed line), followed by a recession period. B - Approximate location of the water table

measured by pressure transducers (red x symbols), linearly interpolated throughout the ERI domain (inner square).

3.2. PERTH results

3.2.1. Data correction procedure and tracer retrieval issues.

The previously described irrigation system issues resulted in a higher than desired variability of the imposed irrigation intensities, which led to an imperfect imposition of PSS conditions. A simple correction procedure was undertaken to circumvent this issue, in that the injection concentration was multiplied by x, where x is the ratio between the average irrigation intensity of each tracer injection divided by the average PSS irrigation intensity. This correction was performed to match the actual tracer input mass and the tracer input mass in "true" PSS.

We have also encountered data quality issues with the measured tracer quantities during the last 2 cycles (not shown in **Figure 3C**) and decided to analyze the data only up to that moment. This led to a total of 10 days of experiment for the proceeding PERTH-based analysis, resulting in the ability to observe ages of water up to 10 days.

3.2.2. PERTH-Based Estimates of S_T and Ω_Q

The SAS components estimated through the PERTH methodology are presented in **Figure 5**. **Figure 5A** displays the values of S_T at each moment within the imposed 48-hour cycle, where colors from dark blue to light green denote low to high storage values, respectively. The observed convex shape of the S_T vectors throughout all storage levels denote a larger portion of younger water in comparison with older water in storage.

Figure 5B shows the retrieved Ω_Q values following the same storage-assigned color scheme. The Ω_Q curves do not reach to 1, indicating imperfect mass recovery (Kim et al., 2016). Most importantly, it is possible to verify a general tendency of decreasing storage (light green towards dark blue) to be associated with a lateral shift in the Ω_Q curves towards the left. This shift suggests that as storage decreases, more water having lower age-ranked storage is being sampled from the domain to leave the system. Conversely, higher storage values are associated with the selection of older water. This behavior has been commonly termed as direct storage effect (DSE), which is the opposite of the ISE, mentioned earlier. While the ISE seems to dominate at the catchment-scale

(Pangle et al., 2017; Benettin et al., 2017; Wilusz et al., 2017; Rodriguez et al., 2018; Kuppel et al., 2020), the DSE has been less reported, and particularly associated with specific catchment processes such as overland flow (Wilusz et al., 2020) while also being observed at the large-scale LEO artificial hillslopes (Kim et al., 2021). While it is tempting to hypothesize what caused the observed DSE based on the PERTH data alone, a more thorough discussion including the ERI portion of the analysis is promoted further in the text.

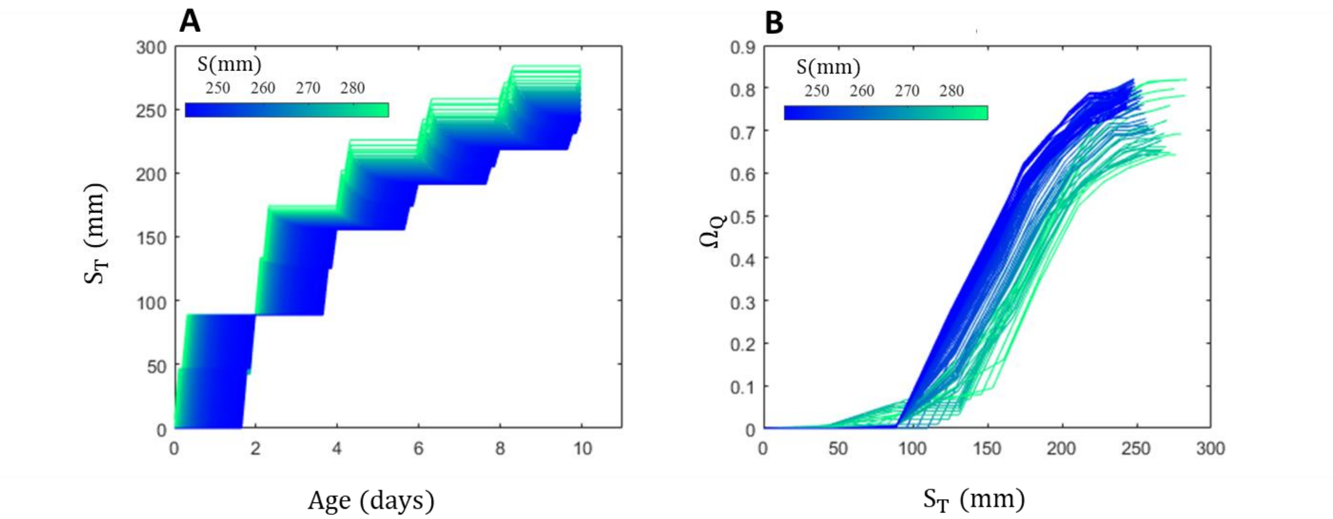

Figure 5. SAS components obtained by the application of the PERTH method over the 48-hours cycle. A –Age ranked storage, S_T, with colors denoting total storage (mm). B – Storage selection functions (Ω_Q) at the discharge, showing the shift towards the selection of waters having lower S_T with decreasing storage.

3.3. Results from the ERI-PSS Method

The ERI-based observation of chloride movement within the lysimeter is discussed here. In section **3.3.1** we discuss how bulk soil conductivity varied within the period prior to the tracer injection (warmup period, i.e., the period where the system was in PSS though irrigation water kept at background concentration), since this is an important aspect precluding the application of the PSS-ERI method for obtaining values of fluid conductivity, as discussed in **2.4.2**. We then move on to the discussion on the lysimeter-scale (as interpolated images along the y-z plane) chloride breakthrough in section **3.3.2**. Information on the validation of the C_{Cl} estimates versus in-situ observations as well as cross-sectional breakthrough images are shown as supporting information (**Text S2, Figures S2 and S3, Table S1**).

3.3.1. Warmup Analysis

Figure 6A shows the average warmup soil-water conductivity ($\bar{\sigma}_{f,W}$) per sampling location for the 3 sampling verticals over cycles 1 through 6. Horizontal bars depict the temporal variability (as one standard deviation) observed throughout the warmup cycles. A gradient of increasing values $\bar{\sigma}_{f,W}$ with soil depth is suggested as a function of distance from the outlet. The pattern of pre-injection fluid conductivities can be attributed to the release of solutes from the basaltic material into solution occurring as the result of geochemical weathering. An analysis performed by Pohlman et al., (2016) on the hydro-geochemical behavior of the LEO hillslopes showed that the regions further from the outlet experience enhanced rates of weathering due to longer rock-water contact times and lower fluxes.

During the warmup period the ERI-acquisition-system faced 2 stoppages, making it impossible to fully observe the cycles 5, 6 and 7. For this reason, we used cycles 1 through 4 for estimation of the pre-injection bulk conductivity values $\sigma_{b,W}$. For the purpose of visualization, **Figure 6B** shows cross-sectional averages of bulk conductivity for those cycles. The repeatability achieved throughout the experiment can be seen as the spike in σ_b values due to the irrigation pulses (represented by the vertical lines), followed by a falling limb, associated with the decrease in soil moisture. It can also be seen that average values increase from the cross-section closest to the outlet (C5) to the cross-section located upslope (C1). This behavior can be attributed to a combination of average moisture contents per cross-section and the observed increase in values σ_f between the outlet and the upper boundary of the lysimeter, as seen in **Figure 6A.**

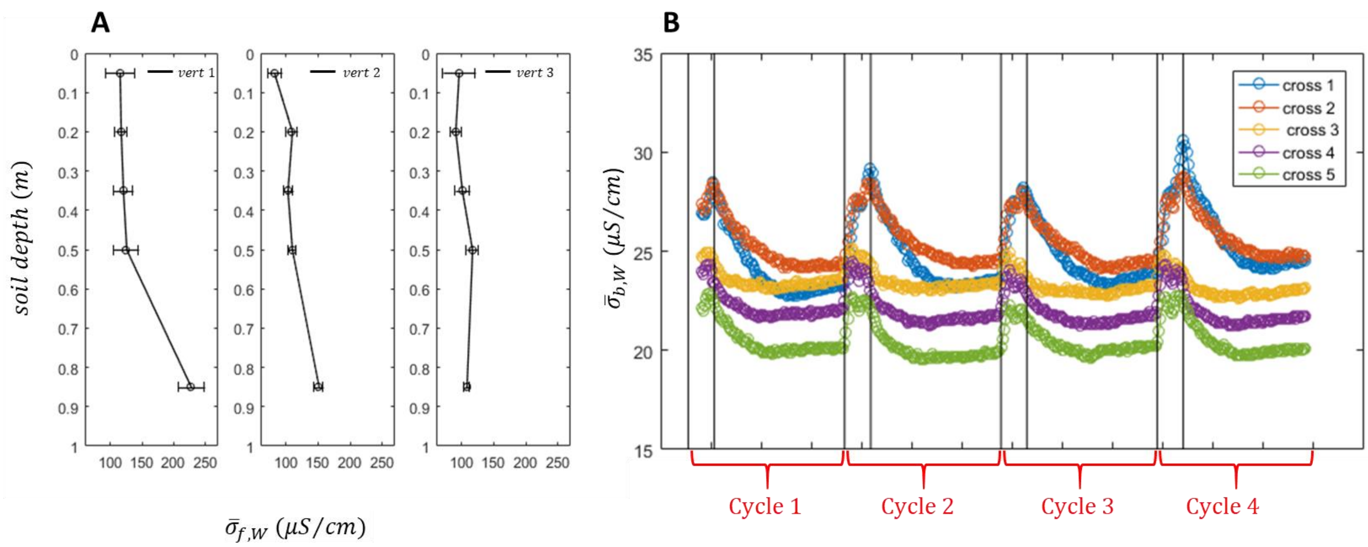

Figure 6. Patterns of bulk soil conductivity and fluid conductivity during warmup. A- Average σ_f obtained for the 3 water sampling verticals from the suction cups for the warmup period. Horizontal bars represent the standard deviation of all measurements taken. The observed low variability in σ_f per sampling led to the choice of constant (average) values in solving for σ_f after injection. B-ERI measurements: cross-sectional averages of σ_b for cycles 1 through 4, used to estimate the pre-injection response. The σ_b trajectories over time illustrate the repeatability of the electrical conductivity as a response to a periodic oscillation of the internal variables. Vertical bars represent beginning and end of irrigation pulses for each cycle.

3.3.2. Lysimeter-Scale chloride Breakthrough

Here, we attempt to reconcile the 2D images of spatially interpolated chloride concentration with the knowledge of the water table fluctuations (as discussed in **3.1**) to further investigate the lysimeter-scale chloride breakthrough, and explain the delayed response in discharge concentration after the first recovery-period irrigation cycle (cycle 9, day 2), as seen in **Figure 3C**. We should note that the final 2D sequence of Cl movement was subject to a manual procedure for the correction of obvious artifacts. This was necessary due to the imperfections in the application of PSS conditions, and possibly the influence of the assumptions on background fluid conductivity. The corrections included removal of subtle oscillations in conductivity located further from the tracer dominated area, substitution of negative conductivity values by 0, and truncation of concentration values to avoid values higher then injection levels.

Figure 7 provides an overlook of both ERI-derived solute movement and water table position at different times for the injection cycle (day 0) and first recovery cycle (day 2). The time stamps shown here were chosen to best represent the temporal dynamics described previously (see **Figure 4**), in which t = 3h represents the first peak in water table at the end of the first irrigation pulse, t = 5h represents an intermediate water table height following a quick 2-hour recession prior to the second pulse, whereas t = 8h represents the water table at its highest level, immediately after the second irrigation pulse. Additionally, **Figure 7G** shows the progression of the chloride concentrations measured at the seepage face, with the timesteps of snapshots shown as vertical bars.

It can be seen that the tracer occupied a well-defined region within the first 25 cm of soil after the second irrigation pulse in day 0 (**Figure 7C).** It is possible to see that no tracer response has been detected at the seepage face for that day whereas the highest water table levels reached for that day were located somewhat far from the tracer-dominated region. On the other hand, on day 2 the tracer plume is pushed down further by the imposed irrigation pulses, allowing for a higher proximity between tracer dominated region and water table, which ultimately lead to the mobilization of the tracer. According to **Figure 7F**, most of the injected solute was placed above the water table at Day2, 8 hr. However, the solute concentration of discharge at that time is already high, which suggests the occurrence of lateral (along the y-direction) flow above the water table in the tension-saturated zone as the main process responsible for the quick tracer mobilization. The absence of an ERI cross-section closest to the seepage makes it impossible to accurately describe the chloride concentrations around that area, but the overall shape of the tracer plume suggests even deeper depths were reached within that region. It is also important to observe the differences between water table heights between both days, in which malfunctioning of the irrigation system being most likely the cause for the lower values of irrigation for day 0, resulting in lower water table levels.

An animation showing the progression of both water table fluctuations and solute movement within the lysimeter is provided (**supporting information Movie#1**) to aid the interpretation of the results.

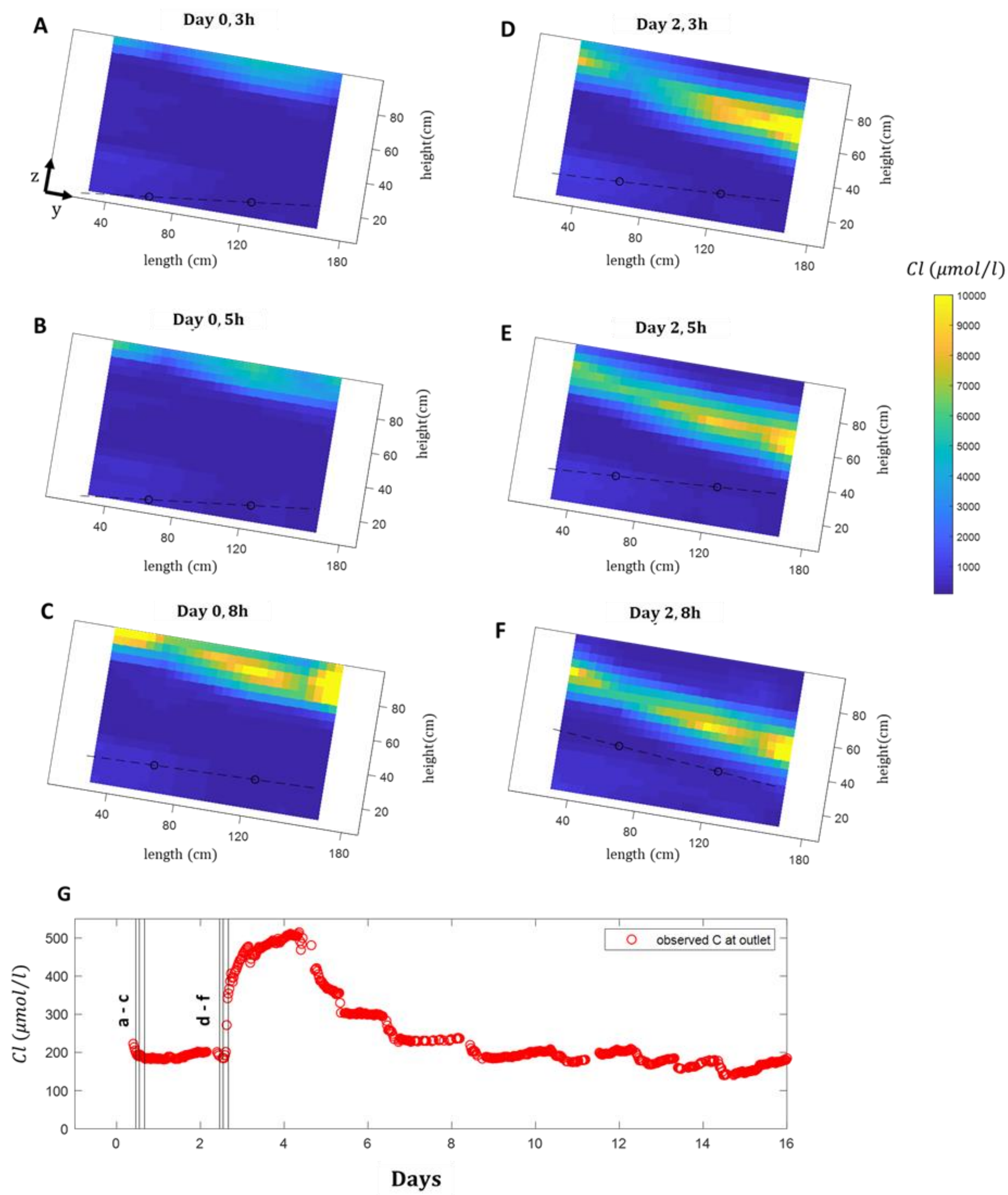

Figure 7. (A-F) Interpolated ERT-derived panels showing chloride concentration in μmol/l throughout days 0 and 2 (tracer injection and following irrigation cycle). Dashed black lines indicate the approximate location of the water table, estimated by pressure transducer measurements at 2 points (circles). G. Estimated chloride concentration from discharge samples, highlighting the time-steps for which the panels A-F were taken.

3.4. ERI-Based Estimates of S_T and Ω_{Q^*}

The SAS components obtained through the ERI-based chloride breakthrough are depicted in **Figure 8**. The predominance of younger water is indicated by the overall convex pattern be observed in **Figure 8A**. The difference in "surveyed" volumes by both methods can be seen when comparing the highest magnitudes of S_T between **Figure 8A** and **Figure 5A,** which is likely due to the fact that the ERI domain does not capture the whole lysimeter, leading to different storage totals. The Ω_{Q^*} functions estimated through ERI (**Figure 8B**) do not display the same smoothness as in the PERTH-based estimation of Ω_{Q^*}, where the shift towards selection of lower values of S_T with decreasing storage values is not as readily observed. Moreover, it can be seen in **Figure 8B** that some curves at the lower storage (dark blue colors) exhibited constant values within certain intervals of S_T. Such pattern can be understood as an indication that certain ranges of S_T were not sampled for those time-steps. Additionally, the ERI-based Ω_{Q^*} seen in **Figure 8B** reach the value of 1. This can be explained by the fact that the changes in age rank storage density estimated within the ERT domain were normalized by the change in storage within the domain (Q^*).

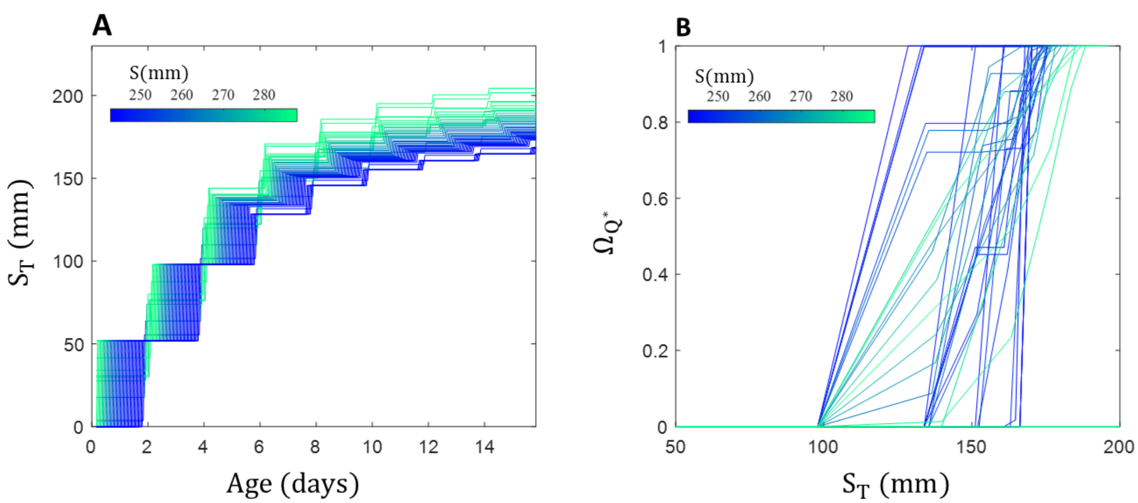

Figure 8- SAS components derived from the pixel-based analysis of ERI images. A – Storage selection functions (Ω_Q) at the discharge, showing the shift towards the selection of waters having lower S_T with decreasing storage.

3.5. Reconciling the Time-Varying SAS Functions and Spatial Distribution of Ages.

Here, we attempt to shed light at the physical mechanisms giving rise to the observed temporal patterns of age-ranked storage and storage selection functions (**Figure 5** and **Figure 8**) throughout the representative cycle. To do so, we extend our analysis to include ERI-based images of water ages and the associated progression of the backwards transit time distribution (bTTD), while also considering the total storage and water table fluctuations.

Figure 9A summarizes the lysimeter's storage (S) and irrigation flux (I) at four distinct moments. The timestamps of 3, 8, 16 and 40 hours were taken to represent the progression of storage caused by the irrigation pulses and discharge out of the lysimeter, as discussed in **3.1** and **Figure 4**. Storage reaches a first peak at 3h as a result of the first irrigation pulse, and is followed by a second, higher peak, at the end of the second irrigation pulse, at 8h. Storage recession starts then, where the 16- and 40-hour labels represent early and late recession moments.

The spatial distribution of water ages within the lysimeter for the 4 different moments are highlighted in **Figure 9B, D, F and H**. These images display the most frequent age value found in each pixel, $\mathcal{T}^*$, with yellow representing older water and dark blue representing younger water. To facilitate the visualization of where each age was most likely to be found throughout the progression of the experiment, we highlighted, in red, the values of water ages at the injection moment for the 3-hour snapshot **Figure 9B (**the actual ages at that moment should be incremented by 3 hours).

Also shown are the approximate water table locations, which will be discussed further in this section. The observation of $\mathcal{T}^*$ values on the left-side images makes some observations possible. A distinctive pattern is clear between all time-steps, in which water with older ages are found at the bottom left region of the lysimeter with mean age values decreasing both towards the lysimeters outlet as well as towards the soil surface. Both vertical and lengthwise patterns were somewhat expected from the chloride breakthrough observed in **Figure 7**: regions that have "seen" the chloride tracer comparatively later than others and where the tracer stayed for longer are assigned higher values of $\mathcal{T}^*$. In other words, longer residence times suggested by the chloride tracer progression were translated into higher values of $\mathcal{T}^*$, whereas more *active* regions are associated with lower $\mathcal{T}^*$ values. It is also possible to notice the effect of the irrigation water being added to the lysimeter as the increase in the extent of the region having low $\mathcal{T}^*$, extending vertically downwards from the soil surface (**Figure 9B and D,** 3 and 8 hours respectively**)**. Additionally, the spatial distribution of $\mathcal{T}^*$ at the later time-step (**Figure 9H**, 40 hours) shows a very similar pattern to the one at 16 hours (**Figure 9F**), the latter having overall lighter hues. This similarity indicates that the depth reached by the water applied with the rainfall did not change noticeably over the drying period, while the effect of ageing of water can be seen in the dimming of the colors.

We then calculated the backwards transit time distribution in its *density* form ($\overleftarrow{p}_Q$) for the same snapshots for a combined analysis of the ages of water being discharged through time. These results can be seen on the right-side, as **Figure 9C, E, G and I.** It is possible to see that the end of the first rain pulse (**Figure 9C**) marks the moment where 2-day old water starts becoming present in the discharge, although in a very small amount. At the end of the second pulse, when the storage (and discharge) is at its highest, we see a greater portion of 2 days-old water being selected (**Figure 9E**). Following that, as the lysimeter starts experiencing ever decreasing storage values, the proportion of 2 days-old water being discharged is then increased in the subsequent moments (**Figure 9E** through **I**).

Note that as time progresses, water once labeled as 2 days old (as seen at the beginning of the cycle) will reach the age of 4 days at the end of the cycle. In this way, at 40 hours, the youngest water being discharged is now closer to being 4 days old, and the overall shape of the $\overleftarrow{p}_Q$ distribution now resembles the configuration seen at the beginning of the cycle (**Figure 9I**). Although less abundant, older water having ages between 6 and 10 days old also appear in the discharge.

The analysis of both water table levels, and internal age distribution can then be used to suggest the mechanisms behind the observed progression of $\overleftarrow{p}_Q$: **Figure 9H and I** can be taken as a snapshot of the initial conditions prior to the first pulse. Prior to the first irrigation pulse, the initial (low) levels of storage lead to the saturation occurring only at a small region around the seepage face (although not detected by the 2 pressure transducers, but necessary to exist in order for discharge to occur) in which water predominantly with ages 4 days and older are present. Although the seepage face region lies outside of the ERI domain, such pattern in older ages is strongly suggested by visual inspection of the color bands at the lower right corner of the surveyed region in **Figure 9H**. Following that, the imposed irrigation causes the water table to rise (**Figure 9B**) increasing the saturated area around the seepage face, which however still discharges water from the same pool of ages. The irrigation water (age = 0 days) however displaces the water near the surface (age = 2 days) downwards. The subsequent irrigation pulse displaces the 2-day-old water further downwards, while also increasing water table levels (**Figure 9D**). This combined effect of downwards movement of 2-day-old water and rising water table levels brings the 2-day-old water closer the saturated region (note the water table line is intersects the region of ages ≈ 2 days) where it begins to be mobilized (**Figure 9B, C, D and E**). The 2-day-old water is then further mobilized during the recession of the water table (**Figure 9F and G**), suggesting a continuing interaction between the 2-day-old saturated region closer to the seepage face. At the end of the cycle, the once 2-day-old region of the domain is now close to being 4-days old. This can be further verified as the distribution of ages in **Figure 9I** can be seen as resulting from a lateral shift applied to the ages in **Figure 9G**. The system is then subject to another cycle, in which the processes described above take place once again. It is also important to note the role the saturated zone likely plays in releasing older water. Due to the distance between the 10 days-old region and the seepage face, the preceding analysis cannot explain the exact timing when such waters will be seen at the seepage face, since its saturation will not be translated into a quick release, as it might have happened with the seepage face region. However, the increase in the extent of the saturated area towards the back of the lysimeter might help its mobilization at later periods.

To facilitate the interpretation, an animation showing the above results is provided as a supplemental material (**supporting information, Movie #2**).

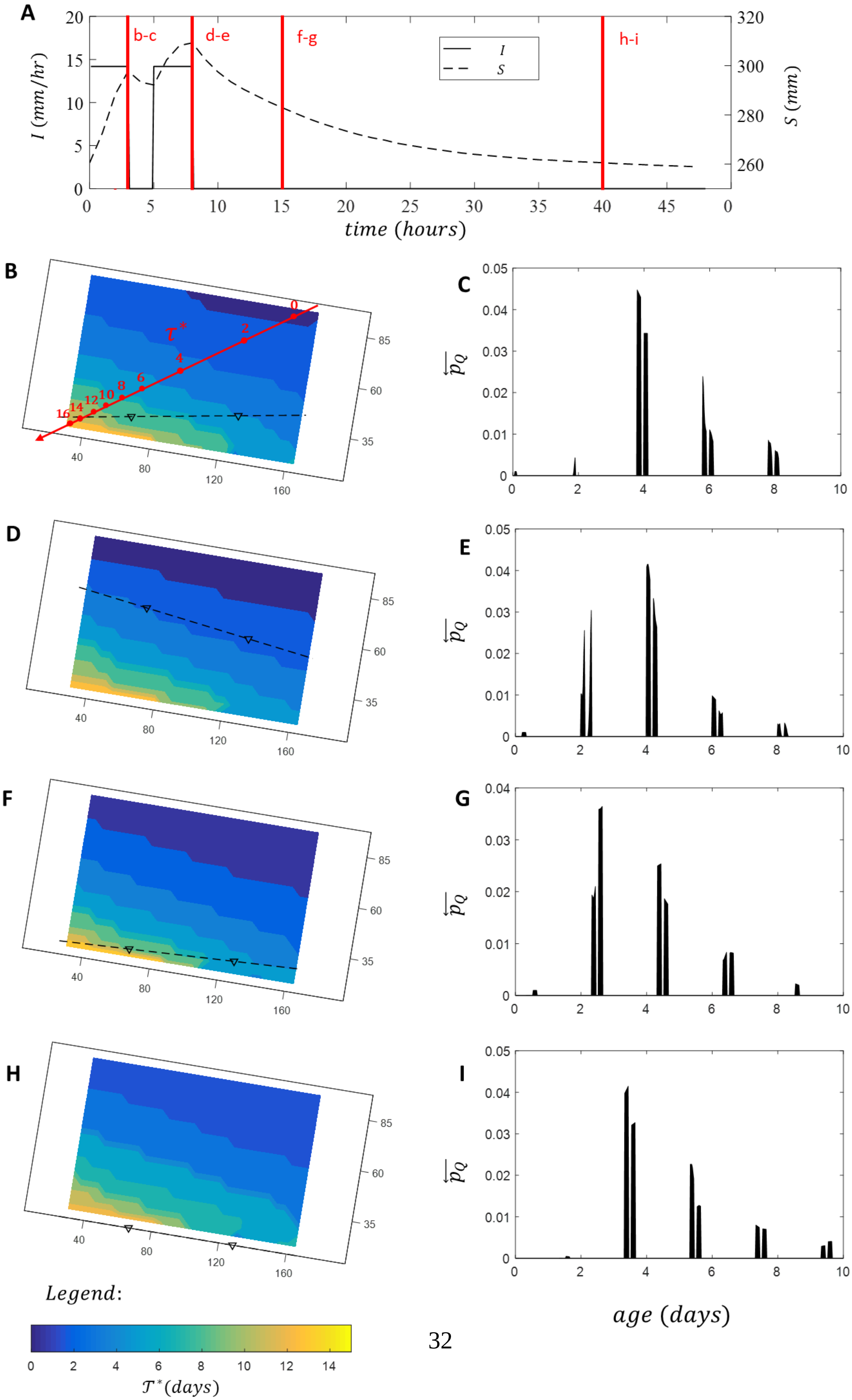

A
I (mm/hr)
S (mm)
time (hours)
b-c
d-e
f-g
h-i
I
S
B
C
D
E
F
G
H
I
$\overrightarrow{p_Q}$
age (days)
Legend:
$\mathcal{T}^*(days)$

727

Figure 9. Evolution of water ages within the lysimeter in comparison with backward-transit-time distributions for 4 distinct moments within the representative cycle. Subplot A shows the moments being depicted in terms of the total storage within the system. Subplots B, D, F and H display the most frequent water age τ^* per pixel. Dashed lines represent the estimated location of the water table throughout the chosen moments. Subplots C, E, G and I display the backwards transit time distribution ($\overleftarrow{p_Q}$) observed at each of the selected moments. Insets are shown to highlight smaller values $\overleftarrow{p_Q}$, associated with older ages (10-14 days-old).

4. Discussion

4.1. Observed Mechanisms Shaping Age Selection.

Our results highlight the interplay between the downward infiltration and the upward saturation resulting in a "layering" of water ages with depth, along with the selection of water ages for discharge being controlled by the spatial and temporal changes in flowpath direction imposed by a dynamic water table. Even though the wetting of the lysimeter led to an extension of the saturated area contributing to discharge, such areas were occupied by pre-event water throughout the whole experiment. We have observed a somewhat constant contribution of pre-event water for most of the wetting period, while fractions of younger water started interacting with the saturated region, and being released, when the lysimeter reached a high storage level. After that, younger water fractions continued being released in an increasing fashion as the water table receded. Even though our surveyed region did not allow for its direct observation, the most likely reason for the continuing release of the younger water with a decreasing water table was the existence of a permanent saturated region closer to the seepage face which might have being reached by the downwards-displaced younger water fraction, allowing for its mobilization.

As mentioned in **3.2.2**, many studies performed at the catchment scale point out to the behavior in which increasing storage is associated with the discharge of younger water (Harman, 2015; Benettin et al., 2017; Wilusz et al., 2017; Kuppel et al., 2020). Fewer investigations have reported the DSE. For example, Wilusz et al., (2020) has shown direct storage effect to be widespread within individual flowpaths, while the catchment as a whole behaves according to an ISE. The authors attribute the seemingly paradoxical finding to the disproportional release of younger water, mainly from overland flow during storms. Similarly, in a recent study performed at the 3 large-scale, LEO artificial hillslopes, Kim et al., (2020) applied the PERTH method and also found the direct storage effect to occur. We think our study can be seen as an example of how a specific catchment unit (in this case a hillslope, or the section of the hillslope closer to the stream, with an impermeable lower boundary) might behave following a DSE.

4.2. Comparison with Previous PERTH Experiment and its Implications

Additional insights about the mechanisms controlling the time-variable SAS components can be gained by comparing the results presented here with other studies applying the PERTH method applied at the same lysimeter (Kim et al., 2016; Pangle et al., 2017). Although the same lysimeter has been used, we should note that it has been destructively sampled (Sengupta et al., 2016) and further repacked between experiments. Most importantly the same basaltic soil was added following the same packing procedure prior to our experiment. Also, the rainfall patterns imposed by the irrigation system did suffer from a slight modification leading to higher rainfall intensities experienced at the lower end of the lysimeter.

Kim et al. (2016) found the system to be characterized by an inverse storage effect. The explanation for the ISE was only broadly hypothesized in the latter study, and further explored through a 2D numerical modeling of solute transport and hydrologic fluxes shown in Pangle et al., (2016). Both studies suggest a rapid mobilization of younger water promoted by the rising water table as the mechanism resulting in the inverse-storage effect.

We believe the characteristics of the hydrologic regime to be one of the main reasons why a different storage effect has been observed. For the experiment of Kim et al., (2016) the PSS cycle consisted of a more intense hydrologic forcing: a 24-hour cycle was imposed, whereas two 4.5 hour-long irrigation pulses were applied with an interval of 7.5 hours in between: the first pulse had a low intensity period (13 mm/hr for 1.5 hour) followed by a high intensity one (26 mm/hr for the remaining 1.5 hour), and the second pulse had a high intensity followed by a low intensity, both having the same duration as in the first pulse. When comparing to the 48-hour cycle applied in this study, a difference of 72 mm in total volume of water added per cycle can be estimated (156 mm versus 84 mm), representing an 86% increase in total irrigation volume, being applied in half of the time. This resulted in a contrasting internal functioning, where a permanent water table (measured at the same locations as in this study**)** of approximately 40 cm was present during dry (low storage) states, which is close to the maximum water table level measured in this study (55 cm). On the other hand, the highest water table seen in Kim et al., (2016) reached levels up to 80 cm during wet periods (high storage). The longer drying periods and an almost complete extinction of the water table between events, together with lower water table levels at wetter conditions precluded the release of event water in our experiment, and also contributed to the delayed discharge of younger water, which occurred predominantly during the recession of the water table, thus characterizing the DSE as suggested by the movement of the Ω_Q function (**Figure 5B**).

The fact that different storage effects can occur through the same basic mechanisms (downward infiltration and water age selection by a dynamic water table), might serve as an evidence on the role of external variability imposed by climate in shaping the SAS functions and the resulting storage effects. Indeed, the results from this experiment align with the commonly held hypothesis of drier systems releasing predominantly older water (Botter et al., 2010; Heidbuchel et al., 2013; Wilusz et al., 2017). We believe the cycle imposed at the lysimeter in this study to be an example of a “drier” regime, whereas the previous experiment (Kim et al., 2016) an example of a “wetter” regime.

Aside from the characteristics of the imposed irrigation cycles, soil structure might also have an important role in explaining the differences in both experiments. Pangle et al., (2016) were only able to reproduce the ISE in their numerical experiment after the inclusion of substantial soil heterogeneity, in which the hydraulic conductivities were assumed to decrease with both depth (along the z-dimension, decreasing from the soil surface downwards), as well as length (along the y-dimension, decreasing towards the seepage face). Such soil heterogeneity was assumed to be caused by soil compaction and was corroborated by actual measurements of bulk density from within the lysimeter (Sengupta et al., 2016). Low hydraulic conductivity values at the bottom-right side of the lysimeter might have contributed to the occurrence of faster flow-paths closer the surface, which would facilitate the export of younger waters as seen in the studies from Kim et al., (2016) and Pangle et al., (2016). The soil used in our experiment was present in the lysimeter for less time and experienced less irrigation cycles. We believe this could have led to less soil compaction, leading to a different soil structure from the one previously reported. The discussion of how different the spatial distribution of soil properties was in our experiment in comparison to the previous PERTH experiment is, however, beyond the scope of this paper and would benefit from numerical experiments as well as the measurement of hydraulic properties, as it has been done previously.

4.3. Limitations and Suggestions for Future Applications

Our findings on the mechanisms ultimately shaping the SAS functions behavior will naturally be subject to the limitations of a controlled, laboratory study. The rainfall regime imposed to the lysimeter was not chosen to represent a specific climate, and the LEO basaltic soil was "engineered" to facilitate the detection of incipient pedogenesis (Pangle et al., 2015). Also, the flat impermeable boundary of the soil lysimeter might not represent commonly observed bedrock features (Gabrielli et al., 2012). Our study can nonetheless stir the discussion on how ages of water observed in the discharge are dynamically linked to internal processes that are universal to many watersheds, as it has provided observational evidence of how both infiltration and saturation from the bottom might interact and determine time-varying SAS functions. As the study of water ages has been many times pursued in saturated versus unsaturated hydrologic compartments (Sprenger et al., 2019), our experiment was able to explore age dynamics in which both spatial and time-varying degrees of saturation occurred.

Some limitations imposed by the ERI procedure used here are also worth discussing. The most important one being that a full-lysimeter picture of the ERI-derived ages of water would be preferred. The extension of the survey to include the whole lysimeter would allow for a better assessment of the lysimeter-scale chloride breakthrough, and a direct comparison between ERI- and PERTH-based results. Due to the strong boundary effects, especially around the seepage face (see how the age-labelled bands tend to "sink" faster closer to the seepage face, in **Figure 9** and **Figure S2**), we believe that actually measured resistivity/conductivity values around the extrapolated regions to be preferred when extending the ERI results into the PERTH analysis. Also, the choice for the acquisition of 2D cross-sectional panels was motivated not only by the constraints imposed by the lysimeter structure onto the location of the electrodes (see Methods Section), but also by time constraints. As mentioned previously, 35 minutes were necessary, on average, for a full scan over the 5 cross-sections. The choice of a 3D survey would invariably increase the survey time, leading to poor temporal coverage of the processes. An ERI system with more channels than what was used here (SuperSting® R8, 8 channels) could allow for a faster image acquisition and therefore the possibility of 3D surveys.

The precision with which the PSS was applied also posed additional challenges for an adequate ERI-based value of Cl concentration. The PSS assumption is of fundamental importance for the estimation of actual σ_f as seen in the normalization procedure shown in **Equation 14**. Equally important is the estimation of background (pre-injection) fluid conductivity values in the same equation. Our spatial estimates were taken by spatial interpolation and extrapolation of observed values at sampling locations (see **Figure 1**). This might have resulted in poor estimation at regions further from the suction cups. While we have attempted to correct clear artifacts in the final images of Cl concentration, through the semi-manual cleaning/filtering procedure described in **3.3.2**, it is not clear whether such procedure was entirely successful to correct for the aforementioned issues.

We believe there is great potential in extending the PERTH method for ERI applications, and that should include applying it at different settings. The procedure as shown here could be tested in other controlled facilities, such as monitored lysimeters, and hillslope transects. The large-scale LEO artificial hillslopes are equipped with ERI capabilities, and the application of the PERTH-ERI method might provide valuable insight into their internal functioning, thus aiding the understanding of water age dynamics at the hillslope scale.

We also envision the application of our method in the field, in which the ERI procedure alone can be followed without the need for validation based on output-based tracer concentration. As provided in the supporting information, a modified procedure should be followed to allow the application of the method on soils with significant surface conduction (mainly soils with clay minerals). Localized sprinkling experiments can provide the necessary PSS conditions at smaller regions to study for example infiltration under different land cover types and the resulting age distribution.

5. SUMMARY

This study presents the results of an experiment to analyze the time-variable TTD in which an output-based tracer sampling allowed for a lumped-system approach and an ERI-based method was used for the estimation of water ages internally. Our system was a 1m^3 sloping soil lysimeter, which allowed for the observation of some hydrologic processes seen at natural hillslopes.

We used the PERTH (Harman and Kim, 2017) method to provide estimates of TTD, which returned in the progression in the ages of water being selected to leave the system as discharge. The PERTH method relies on a rainfall scheme in which a representative hydrologic cycle is repeated several times with tracers being added throughout the experiment and retrieves the progression of TTD within a representative cycle following the SAS framework. We have also introduced the use of ERI as a tool for the investigation of the processes leading to the varying residence times of water. We demonstrated that the PSS theory (Harman and Kim, 2014) can be applied to the equations governing the electrical conductivity of soils to provide a simple solution to the tracer movement under complex conditions. Our method is advantageous over the existing approaches in that it does not require knowledge of petrophysical properties of the material for estimating fluid conductivities that can be applied at transient conditions. The ERI-based method yields additional insights on the time-variability of water ages within the representative cycle and also be used to estimate lumped parameters from the SAS framework.

The results from the combination of both methods promoted a discussion on the internal mechanisms taking place as TTD evolve through time as a function of system storage: As the system experienced two subsequent irrigation pulses, it transitioned from dry (low storage) towards wet (high storage) conditions, followed by a transition from wet to dry (high-to-low storage) as the irrigation stopped. At the first pulse leading to a "wetting" stage the system discharged predominantly older water, whereas as fractions of younger water started being released when the system achieved its highest storage and increased as the system underwent a "drying" stage. This mechanism can be explained by the downwards movement of the younger water being pushed by the applied irrigation alongside with the development of a water table. No event water (i.e. event water being added by the current irrigation pulse) was ever discharged, since the water table did not rise high enough to reach the region with the youngest water. On the other hand, water from the preceding event was released when the region containing waters with that age became saturated, allowing for its quicker mobilization. Since the mobilization started at the moment of highest storage and proceeded with the drying of the system, the system was characterized for the most part as having a direct storage effect.

Our results suggest that the internal assessment of ages to be valuable for unraveling the mechanisms leading to the time-variability of TTD. By comparing our results to a similar study performed at the same system, we were able to hypothesize the controls of climate, seen as the frequency of rainfall events, and the spatial distribution soil properties, as important controls on how ages of water of discharge might be selected from hydrologic systems.

Finally, although this study suffers from the inherent limitations of the system being used, i.e., an artificial hillslope transect, we were able to provide an in-depth analysis of the mechanisms driving water age dynamics that are present in specific watershed units. While the study of water ages is traditionally performed through lumped systems approaches or physically based modelling, the opportunity to directly observe how water ages vary within and out of the domain of interest should be an exciting venue for the advancement of hydro chronology studies.

ACKNOWLEDGEMENTS

Antonio A. M. N. would like to acknowledge the financial support received by the Brazilian Ministry of Education through the CAPES Foundation and the State of Espírito Santo through the FAPES foundation. We would like to thank Ty Ferré (University of Arizona) and Andrew Binley (Lancaster University) on suggestions on electrode design and Michael Tso (Lancaster University) for the support with the program R3. Additionally, the authors would like to thank the Biosphere 2 staff involved in the operational aspects of the experiment: Aaron Bugaj, Nate Abramson, Wei-Ren Ng and Edward Hunt. Upon acceptance, the data used in this study will be available through: https://figshare.com/authors/Antonio_Meira/8292240

REFERENCES

Alumbaugh, D. L., Labrecque, D., Technologies, M., Yeh, T. C. J., De-fg-, G. N., Project, G., & Roland, O. (n.d.). US Department of Energy A HYDROLOGIC - GEOPHYSICAL METHOD FOR CHARACTERIZING FLOW AND TRANSPORT PROCESSES WITHIN THE VADOSE ZONE Project Number : 70267

Ameli, A. A., Amvrosiadi, N., Grabs, T., Laudon, H., Creed, I. F., McDonnell, J. J., & Bishop, K. (2016). Hillslope permeability architecture controls on subsurface transit time distribution and flow paths. *Journal of Hydrology*, *543*, 17–30. https://doi.org/10.1016/j.jhydrol.2016.04.071

Archie, G. E. (1942), The electrical resistivity log as an aid in determining some reservoir characteristics, Trans. Am. Inst. Min. Metall. Pet. Eng., 146, 54–62.

Bellmunt, F., Marcuello, A., Ledo, J., & Queralt, P. (2016). Capability of cross-hole electrical configurations for monitoring rapid plume migration experiments. *Journal of Applied Geophysics*, *124*, 73–82. https://doi.org/10.1016/j.jappgeo.2015.11.010

Benettin, P., C. Soulsby, C. Birkel,D. Tetzlaff, G. Botter, and A. Rinaldo (2017), Using SAS functions and high-resolution isotope data to unravel travel time distributions in headwater catchments, Water Resour. Res., 53, 1864–1878, doi:10.1002/2016WR020117

Binley, A. (2013), R3t, Version 1.8., Lancaster Univ., Lancaster, U. K. (Available at http://www.es.lancs.ac.uk/people/amb/Freeware/Freeware.htm.)

Binley, A., Henry-Poulter, S., & Shaw, B. (1996). Examination of solute transport in an undisturbed soil column using electrical resistance tomography. *Water Resources Research*, *32*(4), 763–769.

Binley, A., Hubbard, S. S., Huisman, J. A., Revil, A., Robinson, D. A., Singha, K., & Slater, L. D. (2015). The emergence of hydrogeophysics for improved understanding of subsurface processes over multiple scales. *Water Resources Research*, *51*, 3837–3866. https://doi.org/10.1002/2015WR017016.Received

Botter, G., Bertuzzo, E., & Rinaldo, A. (2010). Transport in the hydrologic response: Travel time distributions, soil moisture dynamics, and the old water paradox. *Water Resources Research*, *46*(3), 1–18. https://doi.org/10.1029/2009WR008371

Botter, G., Bertuzzo, E., & Rinaldo, A. (2011). Catchment residence and travel time distributions: The master equation. *Geophysical Research Letters*, *38*(11), 1–6. https://doi.org/10.1029/2011GL047666

Brantley, S. L., Goldhaber, M. B., & Vala Ragnarsdottir, K. (2007). Crossing disciplines and scales to understand the critical zone. *Elements*, *3*(5), 307–314. https://doi.org/10.2113/gselements.3.5.307

Campbell, R. B., Bower, C. A., & Richards, L. A. (1948). Change of Electrical Conductivity With Temperature and the Relation of Osmotic Pressure to Electrical Conductivity and Ion Concentration for Soil Extracts. Soil Science Society of America Journal, 13(C), 66–69. https://doi.org/10.2136/sssaj1949.036159950013000c0010x

Cvetkovic, V. (2011). The tempered one-sided stable density: A universal model for hydrological transport? *Environmental Research Letters*, *6*(3). https://doi.org/10.1088/1748-9326/6/3/034008

Danesh-Yazdi, M., Klaus, J., Condon, L. E., & Maxwell, R. M. (2018). Bridging the gap between numerical solutions of travel time distributions and analytical storage selection functions. *Hydrological Processes*, *32*(8), 1063–1076. https://doi.org/10.1002/hyp.11481

Dontsova, K., Steefel, C. I., Desilets, S., Thompson, a., & Chorover, J. (2009). Coupled modeling of hydrologic and geochemical fluxes for prediction of solid phase evolution in the Biosphere 2 hillslope experiment. *Hydrology and Earth System Sciences Discussions*, *6*, 4449–4483. https://doi.org/10.5194/hessd-6-4449-2009

Gabrielli, C. P., McDonnell, J. J., & Jarvis, W. T. (2012). The role of bedrock groundwater in rainfall-runoff response at hillslope and catchment scales. Journal of Hydrology, 450–451, 117–133. https://doi.org/10.1016/j.jhydrol.2012.05.023

Geuzaine, C., Remacle, J. F. (2009). Gmsh: A 3-D finite element mesh generator with built-in pre- and post-processing facilities. *International Journal for Numerical Methods in Engineering*, *79*(11), 1309–1331. https://doi.org/10.1002/nme.2579

Harman, C. J. (2015). Time-variable transit time distributions and transport: Theory and application to storage-dependent transport of chloride in a watershed. *Water Resources Research*, *51*(1), 1–30. https://doi.org/10.1002/2014WR015707

Harman, C. J., and Kim, M. (2014), An efficient tracer test for time-variable transit time distributions in periodic hydrodynamic systems, Geophys. Res. Lett., 41, 1567– 1575, doi:10.1002/2013GL058980.

Heidbüchel, I., Troch, P. a., & Lyon, S. W. (2013). Separating physical and meteorological controls of variable transit times in zero-order catchments. Water Resources Research, 49, 7644–7657. https://doi.org/10.1002/2012WR013149

Jury, W. A. (1982). Simulation of solute transport using a transfer function model. *Water Resources Research*, *18*(2), 363–368. https://doi.org/10.1029/WR018i002p00363

Kemna, A., Kulessa, B., & Vereecken, H. (2002). Imaging and characterisation of subsurface solute transport using electrical resistivity tomography (ERT) and equivalent transport models. *Journal of Hydrology*, *267*, 125–146. https://doi.org/10.1016/S0022-1694(02)00145-2

Kim, M., Pangle, L. A., Cardoso, C., Lora, M., Volkmann, T. H. M., Wang, Y., … Troch, P. A. (2016). Transit time distributions and StorAge Selection functions in a sloping soil lysimeter with time-varying flow paths: Direct observation of internal and external transport variability. *Water Resources Research*, *52*(9), 7105–7129. https://doi.org/10.1002/2016WR018620

Kim, M., Volkmann, T. H., Harman, C., Wang, Y., Troch, P. A. Direct observation of hillslope scale StorAge Selection functions in an experimental hydrologic system: Geomorphologic structure and the preferential discharge of old water. Under review at Water Resources Research. Preprint: https://www.essoar.org/doi/10.1002/essoar.10504485.1

Koestel, J., Kemna, A., Javaux, M., Binley, A., & Vereecken, H. (2008). Quantitative imaging of solute transport in an unsaturated and undisturbed soil monolith with 3-D ERT and TDR. *Water Resources Research*, *44*(12), 1–17. https://doi.org/10.1029/2007WR006755

Kuppel, S., Tetzlaff, D., Maneta, M. P., & Soulsby, C. (2020). Critical zonenstorage controls on the water ages of ecohydrological outputs. Geophysical Research Letters, 47, e2020GL088897. https://doi.org/10.1029/2020GL088897

LaBrecque, D. J., and X. Yang (2001), Difference inversion of ERT data: A fast inversion method for 3-D in situ monitoring, J. Environ. Eng. Geophys., 6, 83-89. https://doi.org/10.4133/JEEG6.2.83

Landon, M. K., Delin, G. N., Komor, S. C., & Regan, C. P. (2000). Relation of Pathways and Transit Times of Recharge Water to Nitrate Concentrations Using Stable Isotopes. *Groundwater*, *38*(3), 381–395.

Looms, M. C., Jensen, K. H., Binley, A., & Nielsen, L. (2008). Monitoring Unsaturated Flow and Transport Using Cross-Borehole Geophysical Methods. *Vadose Zone Journal*, *7*(1), 227. https://doi.org/10.2136/vzj2006.0129

Maher, K. (2010). The dependence of chemical weathering rates on fluid residence time. *Earth and Planetary Science Letters*, *294*(1–2), 101–110. https://doi.org/10.1016/j.epsl.2010.03.010

Maher, K. (2011). The role of fluid residence time and topographic scales in determining chemical fluxes from landscapes. *Earth and Planetary Science Letters*, *312*(1–2), 48–58. https://doi.org/10.1016/j.epsl.2011.09.040

Małoszewski, P., & Zuber, A. (1982). Determining the turnover time of groundwater systems with the aid of environmental tracers. *Journal of Hydrology*, *57*, 207–231. https://doi.org/10.1016/0022-1694(82)90147-0

McDonnell, J. J., McGuire, K., Aggarwal, P., Beven, K. J., Biondi, D., Destouni, G., … Wrede, S. (2010). How old is streamwater? Open questions in catchment transit time conceptualization, modelling and analysis. *Hydrological Processes*, *24*, 1745–1754. https://doi.org/10.1002/hyp.7796

McGuire, K. J., & McDonnell, J. J. (2006). A review and evaluation of catchment transit time modeling. *Journal of Hydrology*, *330*, 543–563. https://doi.org/10.1016/j.jhydrol.2006.04.020

Niemi, A. J. (1977), Residence time distributions of variable flow processes, Int. J. Appl. Radiat. Isotopes, 28(10–1), 855–860, doi:10.1016/0020-708X(77)90026-6

Pangle, L. a., DeLong, S. B., Abramson, N., Adams, J., Barron-Gafford, G. a., Breshears, D. D., … Zeng, X. (2015). The Landscape Evolution Observatory: A large-scale controllable infrastructure to study coupled Earth-surface processes. *Geomorphology*, 1–14. https://doi.org/10.1016/j.geomorph.2015.01.020

Pangle, L. A., Kim, M., Cardoso, C., Lora, M., Meira Neto, A. A., Volkmann, T. H. M., … Harman, C. J. (2017). The mechanistic basis for storage-dependent age distributions of water discharged from an experimental hillslope. *Water Resources Research*, *53*(4), 2733–2754. https://doi.org/10.1002/2016WR019901

Perri, M. T., Cassiani, G., Gervasio, I., Deiana, R., & Binley, A. (2012). A saline tracer test monitored via both surface and cross-borehole electrical resistivity tomography: Comparison of time-lapse results. Journal of Applied Geophysics, 79, 6–16. https://doi.org/10.1016/j.jappgeo.2011.12.011

Pohlmann, M., Dontsova, K., Root, R., Ruiz, J., Troch, P., & Chorover, J. (2016). Pore water chemistry reveals gradients in mineral transformation across a model basaltic hillslope. *Geochemistry, Geophysics, Geosystems*, *17*(6), 2054–2069. https://doi.org/10.1002/2016GC006270

Porporato, A., & Calabrese, S. (2015). On the probabilistic structure of water age. *Water Resources Research*, *51*(5), 3588–3600. https://doi.org/10.1002/2015WR017027

Rinaldo, A., Benettin, P., Harman, C. J., Hrachowitz, M., Mcguire, K. J., Velde, Y. Van Der, … Botter, G. (2015). Storage selection functions: A coherent framework for quantifying how catchments store and release water and solutes. *Water Resourses Research*, *51*, 1–8. https://doi.org/10.1002/2015WR017273.Received

Rodriguez, N. B., McGuire, K. J., & Klaus, J. (2018). Time-Varying Storage–Water Age Relationships in a Catchment With a Mediterranean Climate. *Water Resources Research*, *54*(6), 3988–4008. https://doi.org/10.1029/2017WR021964

Sengupta, A., Wang, Y., Meira Neto, A. A., Matos, K. A., Dontsova, K., Root, R., ... & Troch, P. A. (2016). Soil lysimeter excavation for coupled hydrological, geochemical, and microbiological investigations. Journal of Visualized Experiments, 115, 1-11.

Singha, K., & Gorelick, S. M. (2006). Hydrogeophysical tracking of three-dimensional tracer migration: The concept and application of apparent petrophysical relations. *Water Resources Research*, *42*(6), 1–14. https://doi.org/10.1029/2005WR004568

Slater, L., Binley, a., Versteeg, R., Cassiani, G., Birken, R., & Sandberg, S. (2001). A 3D ERT study of solute transport in a large experimental tank. *Journal of Applied Geophysics*, *49*, 211–229. https://doi.org/10.1016/S0926-9851(02)00124-6

Slater, L., Binley, A. M., Daily, W., & Johnson, R. (2000). Cross-hole electrical imaging of a controlled saline tracer injection. *Journal of Applied Geophysics*, *44*(2–3), 85–102.

Sprenger, M., Stumpp, C., Weiler, M., Aeschbach, W., Allen, S. T., Benettin, P., et al. (2019). The demographics of water: A review of water ages in the critical zone. Reviews of Geophysics, 57. https://doi.org/10.1029/2018RG000633

Turner, J., Albrechtsen, H. J., Bonell, M., Duguet, J. P., Harris, B., Meckenstock, R., … van Lanen, H. (2006). Future trends in transport and fate of diffuse contaminants in catchments, with special emphasis on stable isotope applications. *Hydrological Processes*, *20*(1), 205–213. https://doi.org/10.1002/hyp.6074

Van Der Velde, Y., Torfs, P. J. J. F., Van Der Zee, S. E. A. T. M., & Uijlenhoet, R. (2012). Quantifying catchment-scale mixing and its effect on time-varying travel time distributions. *Water Resources Research*, *48*(6), 1–13. https://doi.org/10.1029/2011WR011310

van der Velde, Y., Heidbüchel, I., Lyon, S. W., Nyberg, L., Rodhe, A., Bishop, K., & Troch, P. a. (2015). Consequences of mixing assumptions for time-variable travel time distributions. *Hydrological Processes*, *29*(16), 3460–3474. https://doi.org/10.1002/hyp.10372

Wherer, M., & Slater, L. D. (2014). Characterization of water content dynamics and tracer breakthrough by 3-D electrical resistivity tomography (ERT) under transient unsaturated conditions. *Water Resources Research*, *50*(7), 5510–5531. https://doi.org/10.1002/2013WR014910.Received

Wilusz, D. C., Harman, C. J., & Ball, W. P. (2017). Sensitivity of Catchment Transit Times to Rainfall Variability Under Present and Future Climates. *Water Resources Research*, *53*(12), 10231–10256. https://doi.org/10.1002/2017WR020894

Wilusz, D. C., Harman, C. J., Ball, W. P., Maxwell, R. M., & Buda, A. R. (2020). Using particle tracking to understand flow paths, age distributions, and the paradoxical origins of the inverse storage effect in an experimental catchment. Water Resources Research, 56, e2019WR025140. https://doi.org/10.1029/2019WR025140

Yang, J., Heidbüchel, I., Musolff, A., Reinstorf, F., & Fleckenstein, J. H. (2018). Exploring the Dynamics of Transit Times and Subsurface Mixing in a Small Agricultural Catchment.